

























## BASSET: Bandpass-Adaptive Single-pulse SEarch Toolkit – Optimized Sub-Band Pulse Search Strategies for Faint Narrow-Band FRBs

J. H. CAO <sup>1,2</sup> P. WANG <sup>1,3</sup> D. LI <sup>4,1,5</sup> Q. H. PAN,<sup>5</sup> K. MAO,<sup>5</sup> C. H. NIU <sup>6</sup> Y. K. ZHANG <sup>1,2</sup> Q. Y. QU <sup>1,2</sup>  
W. J. LU <sup>1,2</sup> J. S. ZHANG <sup>1,2</sup> Y. H. ZHU <sup>1,2</sup> Y. D. WANG <sup>1,2</sup> H. X. CHEN,<sup>5</sup> X. L. CHEN <sup>1</sup> E. GÜGERCINOĞLU,<sup>1</sup>  
J. H. FANG <sup>5</sup> Y. FENG <sup>5,7</sup> H. GAO <sup>3,8</sup> Y. F. HUANG <sup>9,10</sup> J. LI <sup>11</sup> C. C. MIAO <sup>5</sup> C. W. TSAI <sup>1,3,2</sup>  
J. M. YAO,<sup>12</sup> S. P. YOU,<sup>13</sup> R. S. ZHAO <sup>14</sup> Q. Z. LIU,<sup>15,16</sup> S. M. WENG <sup>17</sup> S. H. YEW <sup>17</sup> J. ZHANG,<sup>16</sup>  
L. ZHANG <sup>1,18</sup> D. K. ZHOU <sup>5</sup> AND W. W. ZHU <sup>1,3</sup>

<sup>1</sup>*National Astronomical Observatories, Chinese Academy of Sciences  
20A Datun Road, Chaoyang District, Beijing 100101, China*

<sup>2</sup>*University of Chinese Academy of Sciences  
Beijing 100049, China*

<sup>3</sup>*Institute for Frontiers in Astronomy and Astrophysics, Beijing Normal University  
Beijing 102206, China*

<sup>4</sup>*Department of Astronomy, Tsinghua University  
Beijing 100084, China*

<sup>5</sup>*Zhejiang Lab, Hangzhou, Zhejiang 311121, China*

<sup>6</sup>*Central China Normal University  
Wuhan 430079, China*

<sup>7</sup>*Institute for Astronomy, School of Physics, Zhejiang University,  
Hangzhou 310027, China*

<sup>8</sup>*Department of Astronomy, Beijing Normal University,  
Beijing 100875, China*

<sup>9</sup>*School of Astronomy and Space Science, Nanjing University,  
Nanjing 210023, China*

<sup>10</sup>*Key Laboratory of Modern Astronomy and Astrophysics (Nanjing University), Ministry of Education,  
Nanjing 210023, China*

<sup>11</sup>*Department of Astronomy, School of Physical Sciences, University of Science and Technology of China  
Hefei 230026, China*

<sup>12</sup>*Xinjiang Astronomical Observatory, Chinese Academy of Sciences  
Urumqi 830011, China*

<sup>13</sup>*Key Laboratory of Information and Computing Science Guizhou Province, Guizhou Normal University,  
Guiyang 550001, China*

<sup>14</sup>*Guizhou Provincial Key Laboratory of Radio Astronomy and Data Processing, Guizhou Normal University  
Guiyang 550001, China*

<sup>15</sup>*Purple Mountain Observatory, Chinese Academy of Sciences  
Nanjing 210023, China*

<sup>16</sup>*College of Physics and Electronic Engineering, Qilu Normal University,  
Jinan 250200, China*

<sup>17</sup>*Key Laboratory for Laser Plasmas (MoE), School of Physics and Astronomy, Shanghai Jiao Tong University,  
Shanghai 200240, China*

<sup>18</sup>*Centre for Astrophysics and Supercomputing, Swinburne University of Technology  
P.O. Box 218, Hawthorn, VIC 3122, Australia*

Corresponding author: P. Wang  
E-mail: wangpei@nao.cas.cn

Corresponding author: D. Li  
E-mail: dili@mail.tsinghua.edu.cn

Corresponding author: Q. H. Pan  
E-mail: panqh@zhejianglab.org

## ABSTRACT

The existing single-pulse search algorithms for fast radio bursts (FRBs) do not adequately consider the frequency bandpass pattern of the pulse, rendering them incomplete for the relatively narrow-spectrum detection of pulses. We present a new search algorithm for narrow-band pulses to update the existing standard pipeline, Bandpass-Adaptive Single-pulse SEArch Toolkit (BASSET). The BASSET employs a time-frequency correlation analysis to identify and remove the noise involved by the zero-detection frequency band, thereby enhancing the signal-to-noise ratio (SNR) of the pulses. The BASSET algorithm was implemented on the FAST real dataset of FRB 20190520B, resulting in the discovery of additional 79 pulses through reprocessing. The new detection doubles the number of pulses compared to the previously known 75 pulses, bringing the total number of pulses to 154. In conjunction with the pulse calibration and the Markov Chain Monte Carlo (MCMC) simulated injection experiments, this work updates the quantified parameter space of the detection rate. Moreover, a parallel-accelerated version of the BASSET code was provided and evaluated through simulation. BASSET has the capacity of enhancing the detection sensitivity and the SNR of the narrow-band pulses from the existing pipeline, offering high performance and flexible applicability. BASSET not only enhances the completeness of the low-energy narrow-band pulse detection in a more robust mode, but also has the potential to further elucidate the FRB luminosity function at a wider energy scale.

*Keywords:* fast radio bursts – software: data analysis – methods: data analysis

## 1. INTRODUCTION

Fast radio bursts (FRBs) are short-duration coherent radio transients with high energy (for reviews, see [Petroff et al. \(2019\)](#); [Cordes & Chatterjee \(2019\)](#); [Zhang \(2020\)](#); [Xiao et al. \(2021\)](#); [Zhang \(2023\)](#)). The dispersion measures (DMs) of FRBs far exceed the galactic contributions ([Thornton et al. 2013](#)), indicating an extragalactic origin. The highly variable rotation measures (RMs) suggest that the FRB is surrounded by a dynamic magnetized plasma ([Michilli et al. 2018](#); [Xu et al. 2022](#); [Mckinven et al. 2023](#); [Anna-Thomas et al. 2023](#)).

FRB repeaters are continuously observed ([Spitler et al. 2016](#); [Amiri et al. 2018](#); [Niu et al. 2022a](#)), although more FRBs are one-off events. The luminosity function or energy distribution is essential for revealing the nature of the FRB repeater engines. The complex luminosity functions (e.g., FRB 20121102A ([Li et al. 2021](#)), FRB 20201124A ([Zhang et al. 2022](#)), FRB 20190520B ([Niu et al. 2022a](#)), and FRB 20220912A ([Zhang et al. 2023](#))) imply the existence of multiple radiation mechanisms. The observed luminosity functions are significantly affected by biases at the low-energy end. A more intrinsic luminosity function will be obtained by increasing the detection completeness for low-energy pulses. This is related to the FRB search pipelines.

The standard search pipelines are diverse ([Petroff et al. 2019](#)). The Parkes and the UTMOST telescopes use the HEIMDALL<sup>1</sup>. HEIMDALL employs brute force de-dispersion techniques on GPUs ([Champion et al. 2016](#); [Caleb et al. 2017](#)). The Arecibo and Green Bank surveys have applied the PRESTO<sup>2</sup> ([Ransom 2001](#)), with sub-band de-dispersion techniques ([Spitler et al. 2014](#)). Pulses were identified in the ASKAP telescope utilizing the FREDDA ([Bannister et al. 2017](#)). This pipeline is based on the Fast Dispersion Measure Transform (FDMT) ([Zackay & Ofek 2017](#)). Their single-pulse search algorithms are logically similar, generally following the same steps ([Petroff et al. 2019](#)):

- Preliminary radio frequency interference (RFI) excision: A portion of RFI can be removed before search. Time samples and frequency channels affected by RFI will be masked.
- De-dispersion: Corrects for the dispersion effects caused by cold plasma.
- Extracting a time series: The data are averaged over all frequency band to produce one-dimensional time series.
- Baseline estimation or smoothing: Removes the non-uniform baseline in the time series, which is caused by variations in the mean signal.

<sup>1</sup> <https://sourceforge.net/projects/heimdall-astro/>

<sup>2</sup> <https://www.cv.nrao.edu/~sransom/presto/>

- Normalization: Estimates the noise properties to calculate the signal-to-noise ratio (SNR) of a pulse.
- Matched filtering: Convolves the time series with box-car functions of various lengths to identify pulses wider than a single time sample. Peaks in the de-dispersed, normalized, and convolved time series are reported as candidates.
- Candidate grouping: Clusters single-pulse candidates that are likely related to the same event.
- Post-processing RFI excision: Further RFI excision is performed using the candidate list.

These pipelines have different detection sensitivities for technical reasons. For example, [Gourdji et al. \(2019\)](#) detected 41 pulses, while [Aggarwal et al. \(2021\)](#) detected 134 pulses by using the same observational data for FRB 20121102A.

The Canadian Hydrogen Intensity Mapping Experiment (CHIME) has reported that repeating FRBs have larger pulse widths and narrower bandwidths compared to the one-off events ([Pleunis et al. 2021](#)). Pulses from repeating FRBs tend to occupy only a part of the observation bandwidth. The zero-detection frequency band is also averaged in the `Extracting a time series` step, involving noise and decreasing the SNR of the pulses. A new search algorithm is needed to improve the detection completeness for faint narrow-band pulses.

Sub-band search can partially solve this issue, but it depends on the choice of the sub-bands. [Spitler et al. \(2012\)](#) used a multi-moment technique to quantify the distribution of the pulse intensity across frequencies. This technique is only used for excluding the narrow-band RFI. [Kumar et al. \(2024\)](#) uses a Kalman detector technique to increase the SNR of candidates. The Kalman detector assumes that the spectrum follows a Gaussian process, which is hard to account for the morphologically complex FRB pulses. [Men & Barr \(2024\)](#) established TRANSIENTX, which utilizes the density-based spatial clustering of applications with noise (DBSCAN) algorithm to remove the duplicate candidates. The program is CPU-based, posing an issue for GPU users. Additionally, DBSCAN lacks of being interpretable.

In this paper, we present a new user-friendly search toolkit for PRESTO, the "Bandpass-Adaptive Single-pulse SEArch Toolkit" (BASSET<sup>3</sup>). BASSET significantly improves the detection sensitivity for the narrow-band pulses and has the potential to facilitate the search in broad-band observations. In Section 2, we present the framework and algorithms of BASSET. In Section 3, we perform a test on BASSET by applying it to observational data made by the Five-hundred-meter Aperture Spherical radio Telescope (FAST) ([Nan et al. \(2011\)](#), [Li et al. \(2018\)](#)). In Section 4, we reprocess the FRB 20190520B data collected by FAST using BASSET. In Section 5, we update the results from the previous detection by [Niu et al. \(2022a\)](#), demonstrate a parallel-accelerated version of BASSET, and conduct MCMC simulation experiments. Finally, we provide a conclusion in Section 6.

## 2. THE BANDPASS-ADAPTIVE SINGLE-PULSE SEARCH TOOLKIT (BASSET)

BASSET is a user-friendly update toolkit for PRESTO. BASSET is designed to enhance PRESTO's detection sensitivity for the narrow-band faint pulses. The PRESTO's framework with BASSET is shown in Fig. 1, with the following two steps updated:

- Preliminary RFI excision by using the wavelet transform (WT) techniques (Fig. 1 (b)).
- Extracting a time series without noise involved by the zero-detection frequency band. The system bandpass spectrum is removed firstly (Fig. 1 (c)) as data preparation to load adaptive filter (Fig. 1 (d)).

### 2.1. RFI removal based on wavelet transform

We masked RFI-contaminated data to reduce the number of false-positive candidates. The `rfifind` provided by PRESTO may fail to remove the non-stationary RFI. We then developed a new RFI removal program based on WT, `rfi-mask.py`. This program performs a two-dimensional wavelet decomposition on the dynamic spectrum, removes the components with outlier wavelet coefficients, and generates a mask file like `rfifind.rfi-mask.py` has also been added to the BASSET library.

<sup>3</sup> <https://github.com/caojhNAOC/BASSET>

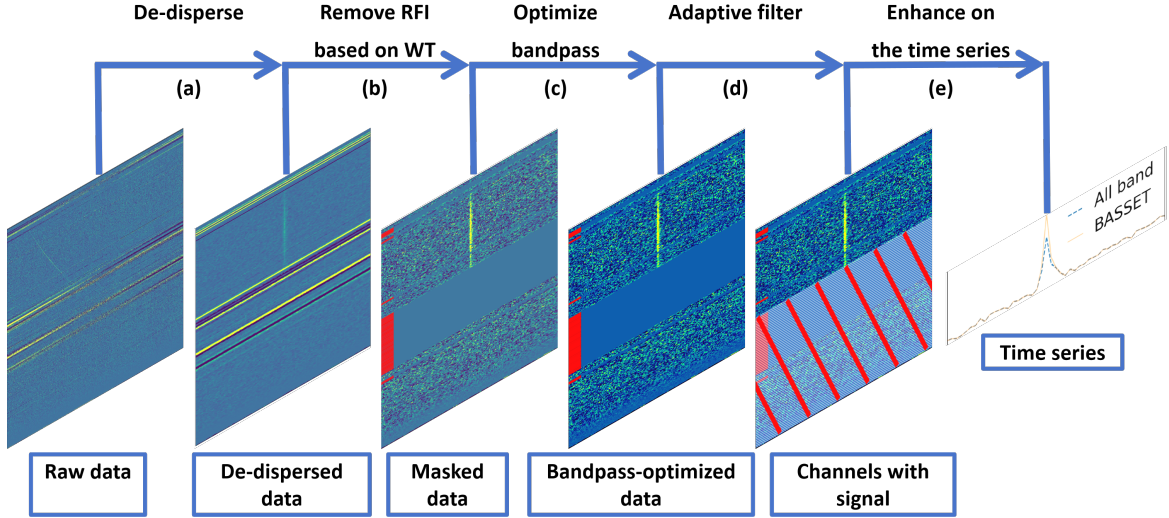


**Figure 1.** The framework of BASSET. The SNR of the narrow-band pulses is improved on the time series using BASSET. The frequency channels affected by RFI are masked and highlighted.

## 2.2. Bandpass optimization

The pulse spectrum in the masked data (Fig. 1) lies on the top of the system bandpass spectrum. The system bandpass spectrum is caused by the sky, ground, and receiver temperatures, and is related to the filters in the receiver chain (O’Neil 2002). The system bandpass spectrum has been removed as data preparation to load adaptive filter. This update has been integrated into the `prepsubband` of PRESTO.

## 2.3. Adaptive filter

We then perform an adaptive filter on the de-dispersed data after masking RFI and optimizing the bandpass. The adaptive filter removes the noise involved by the zero-detection frequency band, leading to an increased significance of the pulse detection. This update has also been integrated into the `prepsubband`. The adaptive filter consists of three steps: `Triggering`, `Searching Time-Frequency Range`, and `Enhancement`. The pulse candidates and their time of arrival (ToA) are obtained based on the bandpass information in the `Triggering` step. Their time-frequency ranges are then localized in the `Searching Time-Frequency Range` step. Subsequently, the SNR of the candidates is improved in the `Enhancement` step. The algorithm for the three steps is as follows:

- `Triggering`:

The spectra of the narrow-band FRB pulses are best described by a box-car or a Gaussian function (Pleunis et al. 2021). We describe the ideal de-dispersed pulse spectral intensity  $I(f)$  as:

$$I(f) = \begin{cases} I_0, & \text{if } CF - BW/2 < f < CF + BW/2, \\ 0, & \text{otherwise,} \end{cases} \quad (1)$$

where  $f$  is the channel index ranging from 0 to  $N - 1$ , and  $N$  is the total number of the frequency channels.  $I_0$  is the characteristic intensity of the pulse.  $BW$  is the bandwidth of the pulse, and  $CF$  is the central frequency of the pulse.

Based on Eq. 1, the adaptive filter performs matched filtering on the data’s bandpass every 5 ms to get the candidates. The matched filtering function  $\mathcal{F}(i)$  is a series of box-car functions:

$$\mathcal{F}(i) = \begin{cases} 1, & \text{if } 0 < i < L, L = L_0, L_1, \dots, L_m, \\ 0, & \text{otherwise,} \end{cases} \quad (2)$$

where  $L$  is the length of the box-car function, and  $L_0, L_1, \dots, L_m$  are a series of trail lengths used to match the pulses with different bandwidths.

The adaptive filter then uses the autocorrelation function (ACF) of the candidates' bandpass to eliminate some false-positive items:

$$ACF(i) = \sum_{k=1}^{N-|N-i|} I_{Cand.}(k) * I_{Cand.}(k + |N - i|), \quad (3)$$

where  $i$  ranges from 0 to  $2N-2$ , and  $Cand.$  is the candidate. The  $ACF$  is symmetric about  $ACF(n)$ . A Gaussian function ( $G(x)$ ) is used to fit the width of the  $ACF$ ,  $W_{ACF}$ :

$$G(x) = Ae^{-\frac{(x-\mu)^2}{2\sigma^2}},$$

with

$$W_{ACF} = 2\sigma. \quad (4)$$

Candidates with  $W_{ACF}$  less than a preset threshold are removed, as  $W_{ACF}$  can serve as an estimate of the candidates' bandwidth.

Eq. (1) is an oversimplified description for the morphologically complex FRB pulses. From a technical point of view, the matched filtering based on the box-car function is computationally effective. The ACF method is model-independent. In astronomy, the ACF has been used to measure pulse drift rates by Marthi et al. (2022).

- Searching for the time-frequency range:

The candidates and their ToAs have been obtained in the **Triggering** step. The  $CF$  of each candidate can be estimated as:

$$CF = \max \text{index}(I_{Cand.} * \mathcal{F}), L = W_{ACF}. \quad (5)$$

To locate the time range of a candidate, the adaptive filter checks the  $W_{ACF}$  and  $CF$  for 1 ms time interval adjacent to the candidate. When

$$|CF_{Cand.} - CF_{Adj.}| < \frac{|W_{ACF} \text{ Cand.} - W_{ACF} \text{ Adj.}|}{2}, \quad (6)$$

this time interval is considered to belong to the time range of the candidate. Here we use  $Cand.$  and  $Adj.$  to distinguish the two  $ACFs$  and  $CFs$ . The next interval is then checked until Eq. (6) is not satisfied.

For a given frequency range, the SNR of the candidate can be expressed as

$$SNR_{Cand.} = \max(TS_{Cand.}) / \text{STD}(TS_{Bg.}), \quad (7)$$

where  $TS$  is the time series by averaging the data over the given frequency range and  $Bg.$  is the background noise data near the candidate. The adaptive filter locates the frequency range giving the maximum SNR,  $SNR_{Cand. \text{ max}}$ , based on Eq. (7).

- Enhancement:

The data within the candidate's time range will be averaged over the localized frequency, increased by a ratio  $\beta$ :

$$\beta = SNR_{Cand. \text{ max}} / SNR_{Cand. \text{ A}}, \quad (8)$$

where  $SNR_{Cand. \text{ A}}$  is the SNR of the candidate averaged over all band.

### 3. TESTING BASSET WITH THE FAST DATA

#### 3.1. BASSET performance on single-component pulses

We selected a sample set of 627 single-component pulses from FRB 20121102A (Li et al. 2021) and FRB 20201124A (Zhou et al. 2022; Zhang et al. 2022; Niu et al. 2022b; Jiang et al. 2022) by utilizing the FAST database **Blinkverse** Xu et al. (2023)<sup>4</sup>. We tested BASSET's performance by applying it to this set. The searched time-frequency ranges

<sup>4</sup> <https://blinkverse.alkaidos.cn/>

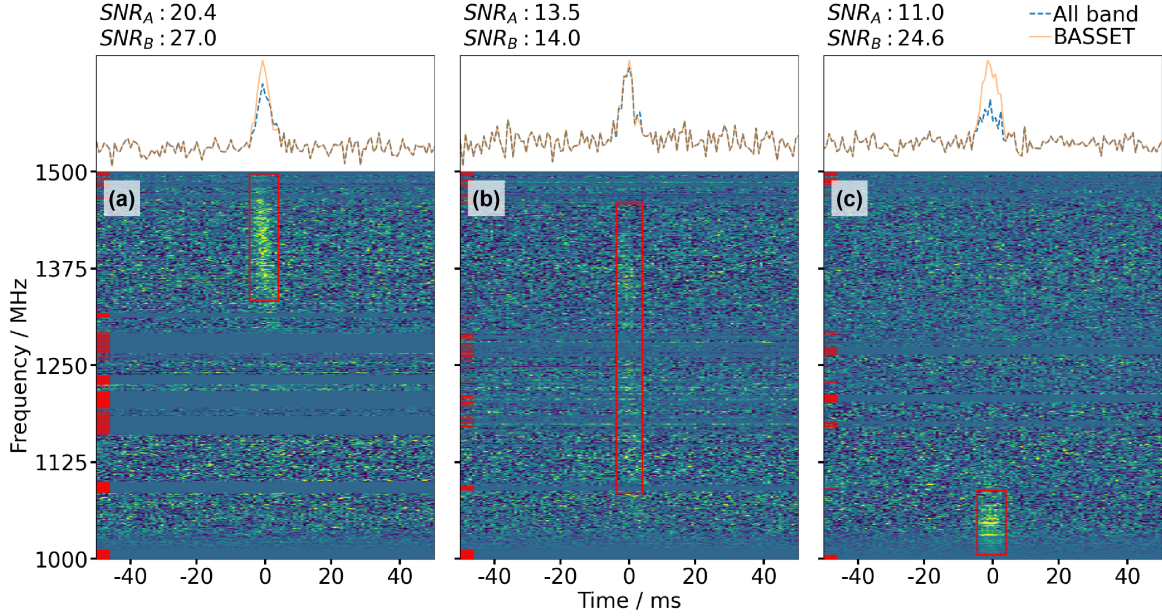


**Figure 2.** The performance of BASSET from application to the three FAST-detected single-component pulses. The pulses in panels a and b are from FRB 20121102A (Li et al. 2021), while the pulse in panel c is from FRB 20201124A. The time-frequency regions searched by BASSET are highlighted with red boxes. The frequency channels affected by RFI are masked and highlighted. The blue dashed line represents the time series processed by the standard pipeline, and the orange solid line represents the time series processed by BASSET.  $SNR_A$  and  $SNR_B$  represent the maximum SNR obtained by the standard pipeline and BASSET, respectively.

are highlighted with red boxes for three of the pulses in Fig. 2. The time series processed by the standard pipeline and BASSET are represented by the blue dashed line and the orange solid line, separately. The two time series are then convolved with a series of trail box-car functions to obtain the maximum SNR reported as  $SNR_A$  and  $SNR_B$ .

BASSET significantly improves the SNR of the narrow-band pulse in Fig. 2, panel c, by the ratio  $SNR_B/SNR_A = 2.24$ . In contrast, this ratio is  $SNR_B/SNR_A = 1.04$ , for the broad-band pulse in Fig. 2, panel b.  $SNR_B/SNR_A$  is aligned with the fraction of the zero-detection band.

We define the “optimized time-frequency range” (hereafter referred to as the “best location”). The pulse yields the maximum SNR ( $SNR_{\max}$ ) when resampled using the best location. We use “best” to denote the best location and “BASSET” to denote the time-frequency range obtained by BASSET. We considered three of typical scenarios based on the bandwidth of the best location ( $BW_{\text{best}}$ ) and the  $SNR_{\max}$ :

- I. 389 pulses with broad bandwidths ( $BW_{\text{best}} > 200$  MHz)
- II. 288 pulses with narrow bandwidths ( $BW_{\text{best}} < 200$  MHz)
- III. 29 pulses with narrow bandwidths ( $BW_{\text{best}} < 200$  MHz) and low SNR ( $SNR_{\max} < 15$ ).

From a technical point of view, we need to compare the differences between the time-frequency range obtained by BASSET and the best location. We use the following residual to quantify the accuracy of the **Searching time-frequency range**:

$$\Delta BW/BW_{\text{best}} = \frac{BW_{\text{BASSET}} - BW_{\text{best}}}{BW_{\text{best}}}, \quad (9)$$

and

$$\Delta W/W_{\text{best}} = \frac{W_{\text{BASSET}} - W_{\text{best}}}{W_{\text{best}}}, \quad (10)$$

where  $W$  is the width of the time range. The total residual  $r_{\text{total}}$  is:

$$r_{\text{total}} = \sqrt{(\Delta BW/BW_{\text{best}})^2 + (\Delta W/W_{\text{best}})^2}. \quad (11)$$

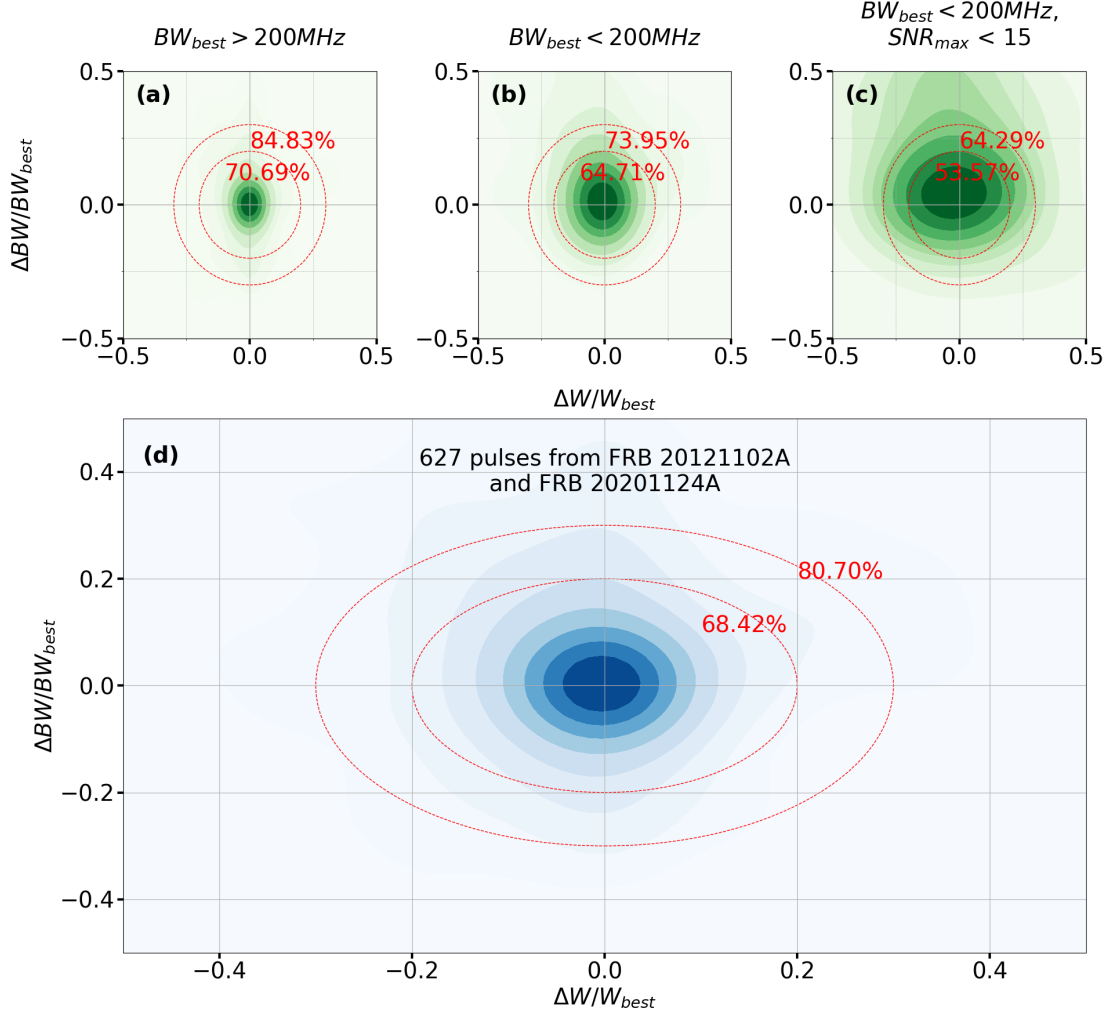


**Figure 3.** The accuracy of Searching time-frequency range is quantified using a 2D KDE of the residuals. Panels a, b, and c show the results of the sample subsets with different bandwidths and SNR. Panel d shows the result of the entire sample set. The percentages of samples with total residuals within 0.2 and 0.3 are shown in red.

We use  $SNR_{max}$  to estimate the uncertainty ( $\epsilon$ ) of the best location:

$$\epsilon = \frac{1}{\sqrt{SNR_{max}}}. \quad (12)$$

The residual will be scaled by the  $\lambda$  factor given by

$$\lambda = 1 - \frac{\epsilon}{r_{total}}. \quad (13)$$

The residual can be ignored when  $\lambda < 0$ , as it is within the uncertainty range. In Fig. 3, we visualized the residuals of 627 pulses by using the two-dimensional kernel density estimation (2D KDE). According to the radiometer equation, we can estimate:

$$\begin{cases} \lambda r_{total} < 0.2, SNR_B \geq 90\% SNR_{max} & \text{for 68.42\% completeness} \\ \lambda r_{total} < 0.3, SNR_B \geq 84\% SNR_{max} & \text{for 80.70\% completeness} \end{cases} \quad (14)$$

Most of the outlier residual structure in Fig. 3, panel d is attributed to the frequency drifting or scintillation, leading to blurring the pulse morphology.

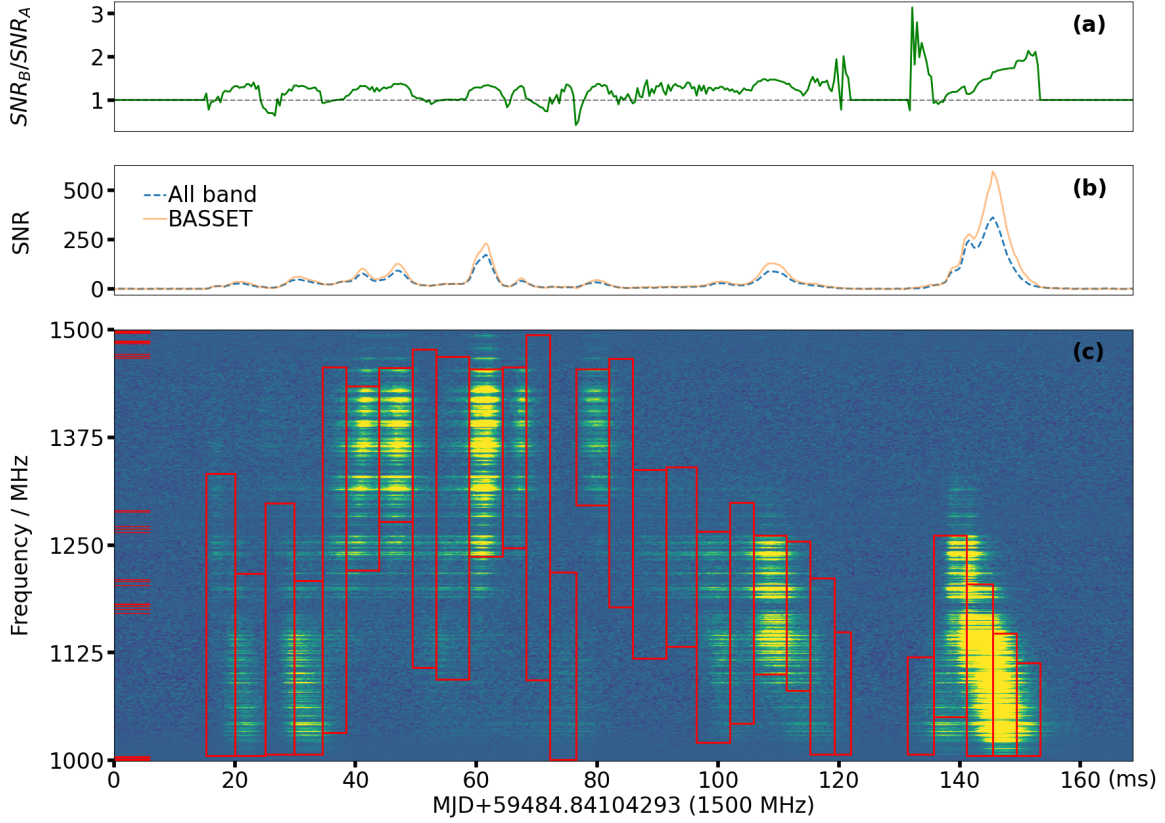


**Figure 4.** The performance of BASSET when applied to a series of morphologically complex pulses from FRB 20201124A. Panel a shows the  $SNR_B/SNR_A$ . In panel b, The blue dashed line represents the time series processed by the standard pipeline, and the orange solid line represents the time series processed by BASSET. Panel c shows the dynamic spectrum of the pulses. The time-frequency regions searched by BASSET are highlighted with red boxes. The frequency channels affected by RFI are masked and highlighted.

### 3.2. BASSET performance on complex-structured pulses

We selected a series of morphologically complex pulses from FRB 20201124A to test the performance of BASSET. The time-frequency ranges searched by BASSET are shown in Fig. 4. BASSET demonstrates a series of promising candidates, covering all of the pulses (Fig. 4, panel c). The detection significance of the pulses is enhanced, with  $SNR_B/SNR_A > 1$  (Fig. 4, panel a). This demonstrates the flexibility of BASSET when applying to the morphologically complex pulses.

### 3.3. BASSET performance in RFI-contaminated environment

In order to test the robustness of BASSET, we designed an experiment by injecting mock pulses into the FAST real data with complicated noise backgrounds. Three typical RFI modes in FAST data are considered (Fig. 5):

- I.** Calibration noise diode across all band (Panel a). The injected pulse has a width of 5 ms, a bandwidth of 300 MHz centered at 1250 MHz, both with a Gaussian shape, and a fluence SNR of 60 (across all band without removing RFI). BASSET will miss pulses with lower SNR in the **Triggering** step, as the spectral intensity is affected by the noise.
- II.** The stationary narrow-band RFI (Panel b). The injected pulse has the same width and bandwidth as Panel a, but with an SNR of 10.
- III.** The narrow-band RFI like a faint bulge (Panel c). The injected pulse is the same as in panel b, except that the central frequency is changed to 1150 MHz.

BASSET successfully locates the pulse range and enhances the significance of detection in the three scenarios. The **Triggering** step will fail for faint pulses in mode I, indicating that this step is sensitive to the spectral intensity of



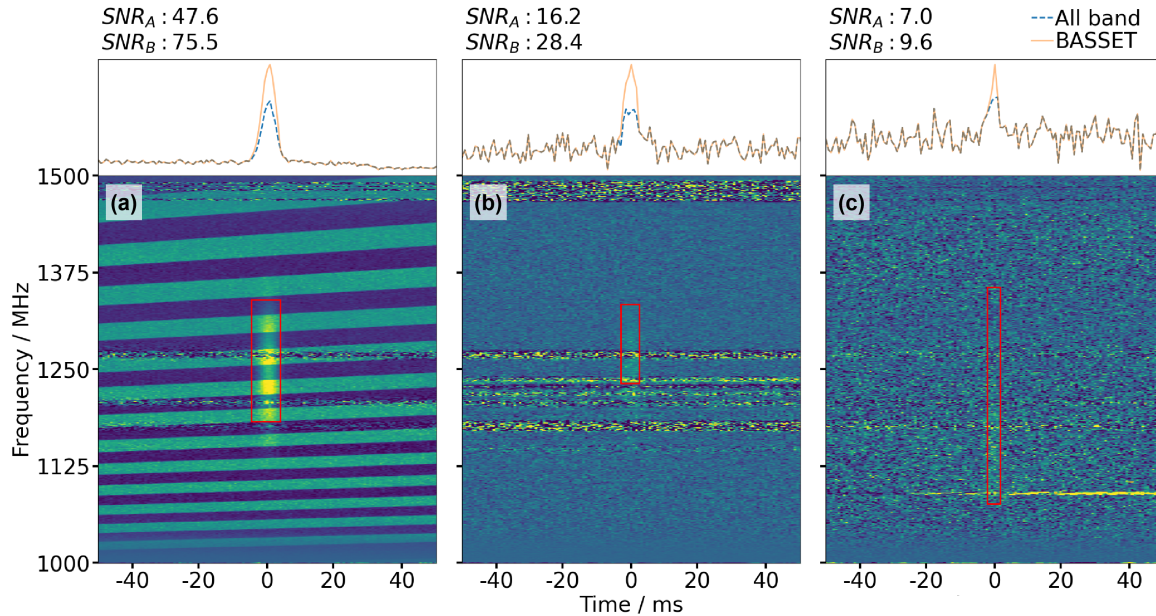


**Figure 5.** BASSET performance in three typical RFI mode environments. Panel a: Calibration noise diode. The injected mock pulse has a width of 5 ms and a bandwidth of 300 MHz centered at 1250 MHz, both with a Gaussian shape, and an fluence SNR of 60. Panel b: The stationary narrow-band RFI. The injected mock pulse has the same width and bandwidth as panel a, but with an SNR of 10. Panel c: The narrow-band RFI like a faint bulge. The injected mock pulse is the same as in panel b with the central frequency changed to 1150 MHz. The time-frequency regions searched by BASSET are highlighted with red boxes.

**Table 1.** The properties of the six newly detected pulses displayed in Fig. 6.  $BW_{\text{Obs.}}$  is the observation bandwidth. More detailed pulse properties are shown in Table 4.

Pulse Num	Bandwidth (MHz)	$BW/BW_{\text{Obs.}}$ (%)	$SNR_B$	$SNR_A$
10	$130^{+13}_{-13}$	26	8.3	3.5
15	$131^{+13}_{-13}$	26	7.3	6.4
38	$147^{+15}_{-15}$	29	10.3	3.6
56	$365^{+67}_{-67}$	73	17.0	12.1
68	$194^{+19}_{-19}$	39	6.7	5.6
70	$121^{+12}_{-12}$	24	18.4	11.7

the pulses. The  $SNR_B$  decreases to 79.13%, 58.57%, and 71.85% for modes I-III, respectively, compared to the  $SNR_B$  obtained in a clean noise background. This percentage is aligned with the fraction of the band contaminated by RFI.

#### 4. REPROCESSING FAST OBSERVATION DATASET OF FRB 20190520B

FAST observations of FRB 20190520B between April and September 2020 were processed using a Heimdall-based pipeline (Niu et al. 2022a). Candidates with  $SNR_A > 7$  were recorded, and 75 pulses were detected in 18.5 hours. There may be missing pulses due to the high detection incompleteness of Heimdall for narrow-band faint pulses. We reprocessed the data using BASSET. Candidates with  $SNR_B > 5$  were recorded, and pulses were manually selected using the dynamic spectrum. The new detection doubles the number of pulses, bringing the total number of pulses to 154. Six of the newly detected pulses are displayed in Fig. 6 and the properties of them are shown in Table 1.

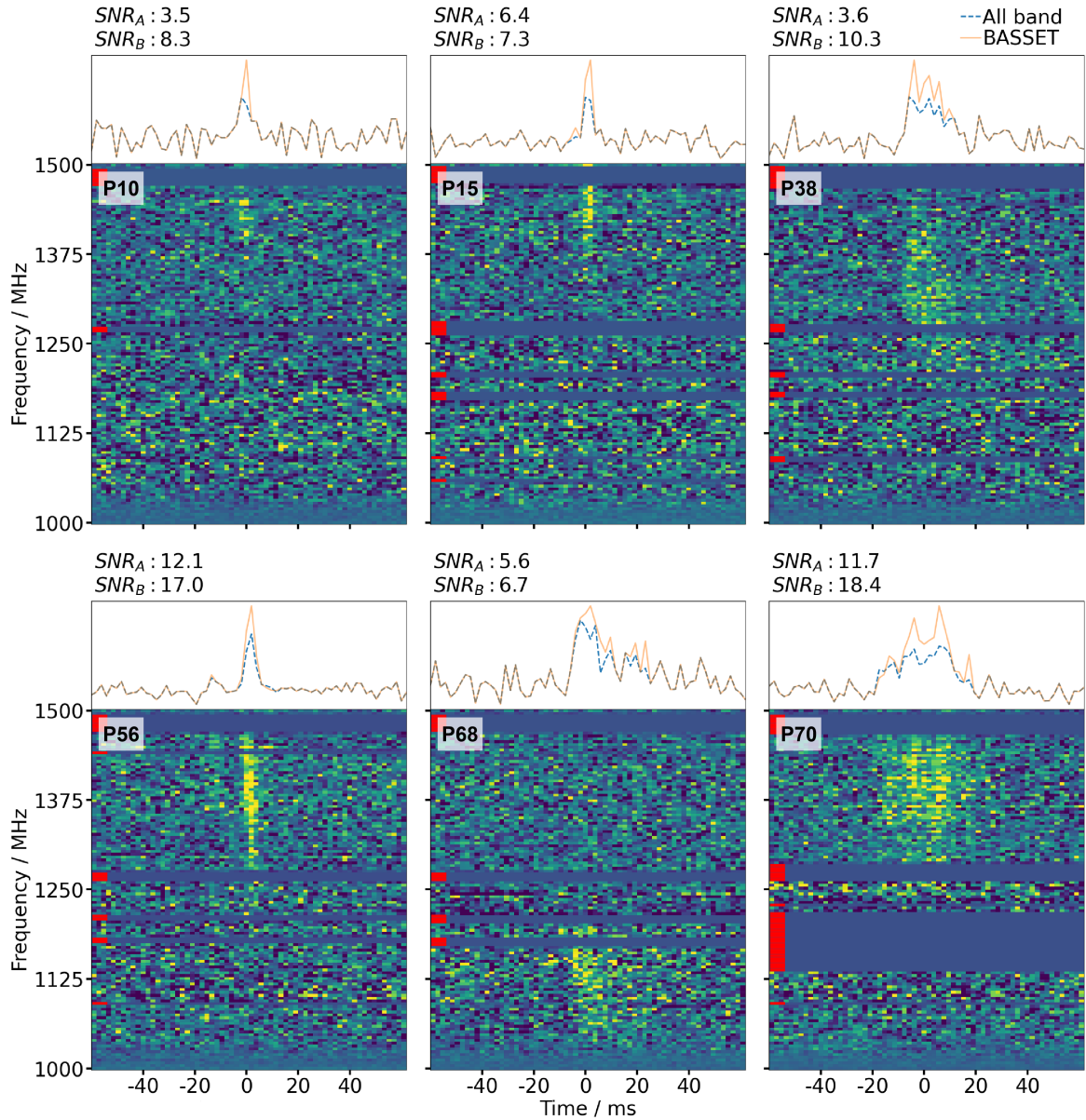


**Figure 6.** A gallery of the newly detected pulses from FRB 20190520B data reprocessing. The  $SNR_A$  is obtained by searching the time series processed by the standard pipeline (blue dashed line), using `single_pulse_search.py` from PRESTO.  $SNR_B$  is obtained by searching the time series processed by BASSET (orange solid line). The frequency channels affected by RFI are masked and highlighted.

Fifty of pulses with  $SNR_A > 5$  missed in the previous search are found by us this time, possibly because we chose a lower SNR threshold. The detection of 29 pulses with  $SNR_A < 5$  clearly demonstrates the improved detection sensitivity using BASSET.

The bandwidth and SNR distribution of the newly detected pulses with a comparison to the previous detection by Niu et al. (2022a) are shown in Fig. 7. The pulses from FRB 20190520B tend to have narrow emission bandwidths (Fig. 7, panel a). The standard pipelines are likely to miss narrow-band faint pulses (Fig. 7, panel b), as suggested by the 49 of newly detected pulses with  $SNR_A < 10$  and  $BW < 200$  MHz.

## 5. DISCUSSION

### 5.1. The energy distribution of FRB 20190520B

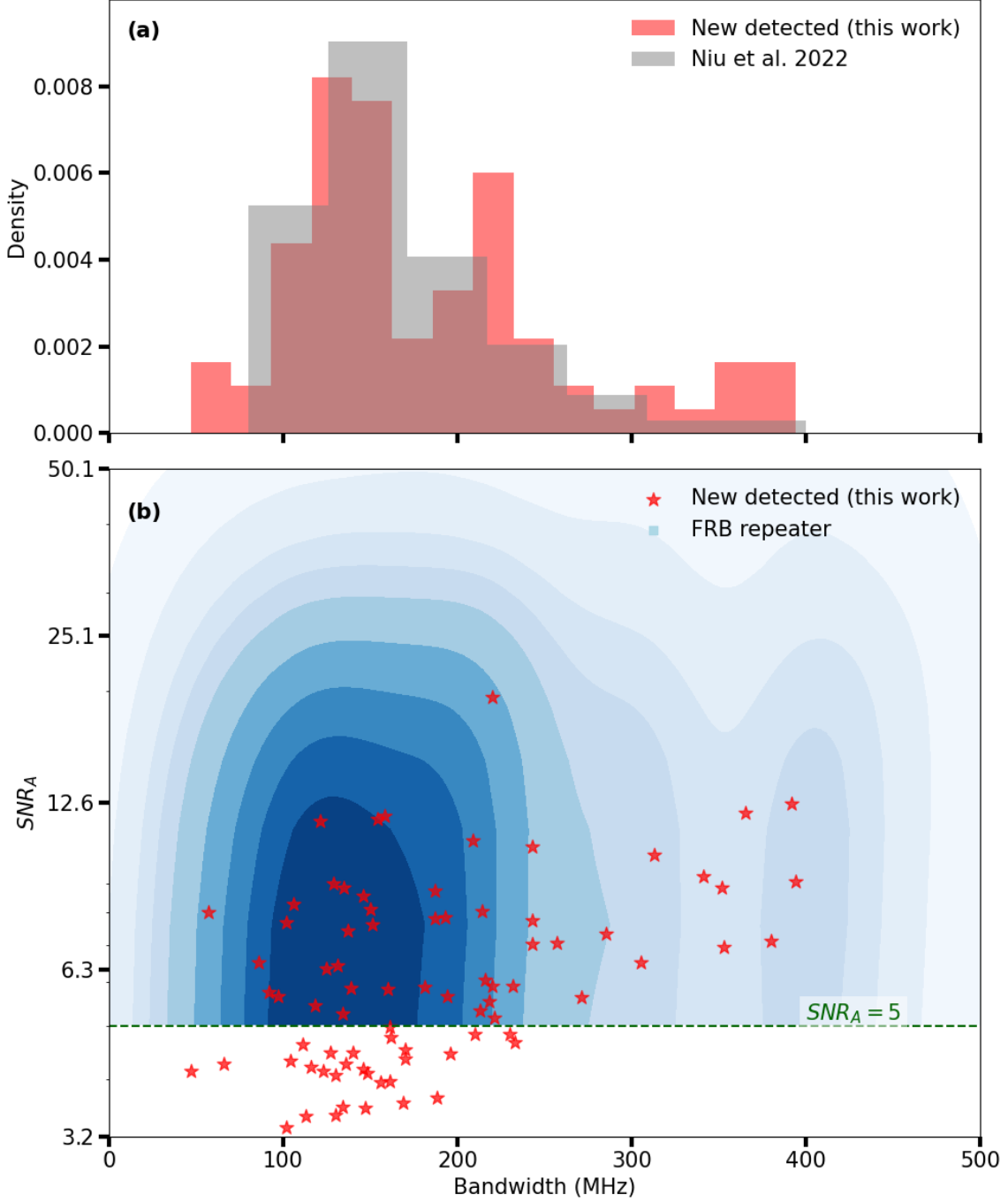


**Figure 7.** The bandwidth and SNR distribution of the newly detected pulses. Panel a shows the bandwidth histogram of the newly detected pulses by BASSET, compared to the previous detection by [Niu et al. \(2022a\)](#). Panel b shows the bandwidth-SNR statistics. The newly detected pulses are marked with red stars, compared to the 2D KDE distribution of FRB 20121102A ([Li et al. 2021](#)), utilizing the FAST database `Blinkverse` ([Xu et al. 2023](#)). Other FRB repeaters are not considered due to the lack of SNR or bandwidth data.

We updated the energy distribution of the FRB 20190520B reported by [Niu et al. \(2022a\)](#) using the new detection set. Following [Niu et al. \(2022a\)](#), we used equation (9) of [Zhang \(2018\)](#):

$$E = 10^{39} \text{ erg} \times \frac{4\pi}{(1+z)} \left( \frac{D_L}{10^{28} \text{ cm}} \right)^2 \left( \frac{F_\nu}{\text{Jy} \cdot \text{ms}} \right) \left( \frac{\nu_c}{\text{GHz}} \right). \quad (15)$$

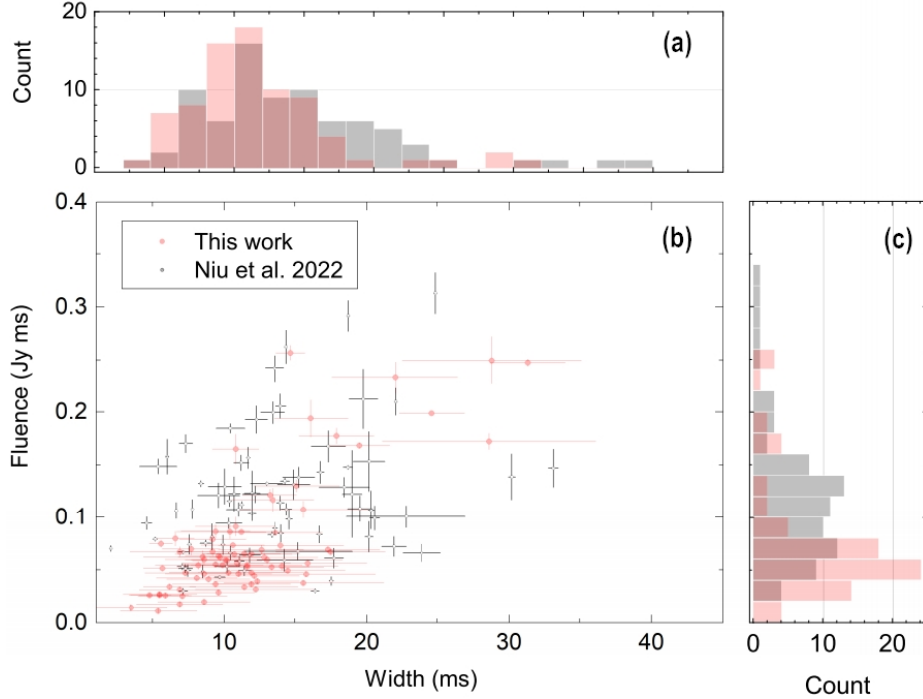


**Figure 8.** The fluence-width distribution of the FRB 20190520B. The red dots and histograms are newly detected 79 pulses using BASSET, while the grey dots and bars are taken from Niu et al. (2022a).

The specific fluence  $F_\nu$  is expressed in units of  $\text{Jy} \cdot \text{ms}$ , measured over the full observation bandwidth. Based on the standard cosmological parameters (Macquart et al. 2020), the luminosity distance for FRB 20190520B is  $D_L = 1.218 \text{ Mpc}$ , corresponding to a redshift of  $z = 0.241$ . The observation center frequency is  $\nu_c = 1.25 \text{ GHz}$  for FAST. The fluence-width distribution is shown in Fig. 8 and the luminosity function is presented in Fig. 9. The luminosity function of FRB 20190520B still exhibits a single modal distribution, suggesting that this may be intrinsic.

### 5.2. Parallel-accelerated version

We implemented a GPU plus OpenMP parallelized version of BASSET to accelerate the FRB search process. We utilize GPU acceleration to parallelize the `De-dispersion` step and various computations within the `Triggering` step, including the optimizing calculation, matched filter calculation, and spectrum ACF calculation. For the Gaussian function of the `Triggering` step and `Searching time-frequency range` step, OpenMP is applied to accelerate the computation on multicore CPUs.

We compared the performance of our parallelized version with the non-parallelized version of BASSET. The test was performed on a GPU server with 20 Intel i7-12700K cores and one NVIDIA A100-PCIE-40GB GPU, and the software environment was Ubuntu 18.04 with CUDA 11.7. We selected a 140-second segment of real FAST data without pulses, which is single-polarized with a sample time of  $98.304 \mu\text{s}$  and 4096 frequency channels. The overall performance of the parallelized version showed a 5.98X speedup compared to the non-parallelized version, as shown in Table 2. The parallel performance of each part in the parallel-accelerated version is shown in Table 3.

### 5.3. Comparison between the BASSET and the PRESTO

In conjunction with pulse calibration and MCMC simulated injection experiments, we update the quantified parameter space of the detection rate for BASSET, compared to the standard pipeline. The injected mock pulses are Gaussian-shaped in both time and frequency, and are injected into a background of Gaussian noise. The parameters for the 2000 injected mock pulses are as follows:

- **Fluence SNR** (Uniform distribution):

– Minimum value: 1

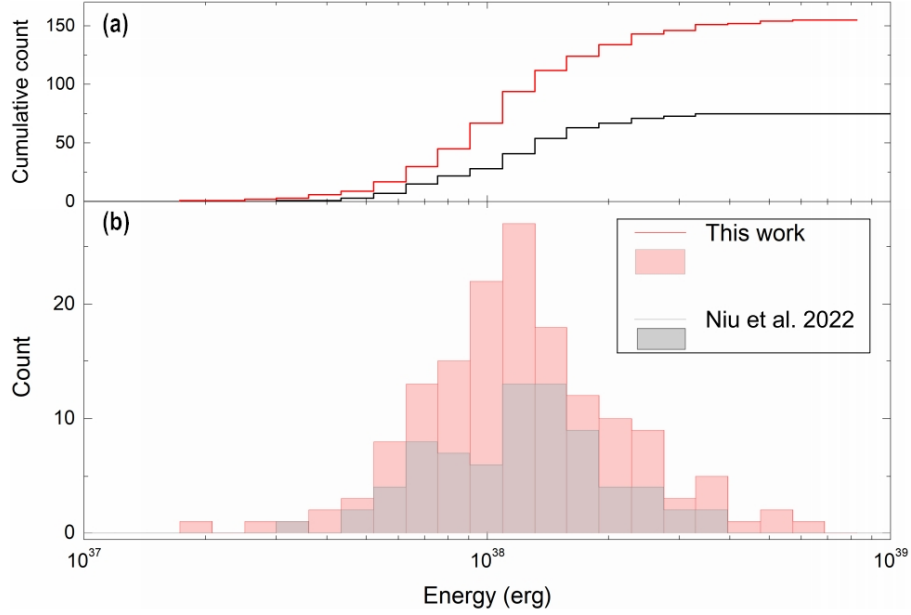


**Figure 9.** The luminosity function of the FRB 20190520B. The red line and bars represent the 79 newly detected pulses using BASSET, while the grey line and bars are taken from Niu et al. (2022a).

**Table 2.** Comparison of the speed time between the standard pipeline (PRESTO) and the BASSET.<sup>a)</sup>

Method	Speed Time
	(s)
PRESTO	91.28
BASSET(non-parallelized)	800.45
BASSET(parallelized)	133.91

*a)* 140-second real FAST data (single-polarized, with a sample time of 98.304  $\mu$ s and 4096 frequency channels) without any pulses is used for testing. The test environment consisted of a GPU server with 20 Intel i7-12700K cores and one NVIDIA A100-PCIE-40GB GPU, running on Ubuntu 18.04 with CUDA 11.7.

**Table 3.** The parallel performance of each part in the parallelized version.<sup>a)</sup>

Step	BASSET	BASSET	Improvement
	(non-parallelized, s)	(parallelized, s)	
De-dispersion of Data <sup>b)</sup>	258.79	10.26	25.22x
Triggering <sup>c)</sup>	345.34	27.10	12.74x
Searching Time-Frequency Range <sup>c)</sup>	140.34	41.38	3.39x

*a)* 140-second real FAST data (single-polarized, with a sample time of 98.304  $\mu$ s and 4096 frequency channels) without any pulses is used for testing. The test environment consisted of a GPU server with 20 Intel i7-12700K cores and one NVIDIA A100-PCIE-40GB GPU, running on Ubuntu 18.04 with CUDA 11.7.

*b)* Corresponding to "De-disperse" in the framework (Fig. 1).

*c)* Corresponding to "Adaptive filter" in the framework (Fig. 1).

- Maximum value: 11
- **Pulse Width** (Lognormal distribution):
  - Mean: 3 ms
  - STD: 2 ms
- **Bandwidth** (Normal distribution):
  - Mean: 150 MHz
  - STD: 100 MHz
- **Central Frequency** (Normal distribution):
  - Mean: 1250 MHz
  - STD: 100 MHz

The SNR of the mock pulses is close to the detection limit, as these pulses are likely to be missed during the search.

The experimental results are shown in Fig. 10. BASSET detected 1379 of the mock pulses whereas the standard pipeline detected 1005 of the pulses, with a detection threshold of  $SNR = 5$ . BASSET enhanced the SNR of 90.91% of the 1002 pulses detected by both methods (Fig. 10, panel a). Some faint pulses were missed in the **Triggering** step, resulting in no enhancement. The enhancement ratio  $SNR_B/SNR_A \approx 2.28$  (Fig. 10, panel c) is consistent with the expected bandwidth (150 MHz). The 90% completeness threshold was set from fluence SNR 7.5 to 6.0 using BASSET (Fig. 10, panel b).

## 6. CONCLUSION

The current single-pulse search algorithms for FRBs are insufficient for the detection of narrow-band pulses due to their failure to account for the frequency bandpass pattern of the pulse. In this paper, we present a new search algorithm, BASSET, which has been developed to enhance the existing standard pipeline for the detection of narrow-band pulses. The FAST data for FRB 20190520B were reprocessed using BASSET, and the results of the previous detection by Niu et al. (2022a) were updated.

- We designed BASSET, a user-friendly single-pulse search toolkit for PRESTO, along with a parallel-accelerated version. BASSET significantly enhances the detection sensitivity of PRESTO for narrow-band faint pulses. PRESTO users can utilize the BASSET by replacing `prepsubband` with `prepsubband-BASSET`, and `rfifind` with `rfi-mask.py`.
- We conducted a series of experiments based on FAST real data reprocessing and MCMC simulations to test the performance of BASSET. BASSET enhances the SNR of pulses with different time-frequency morphological structures and demonstrates robustness for complex RFI environments. The BASSET search pipeline is more sensitive than the full-band search pipelines, and has established a 90% completeness threshold, which has lowered the fluence SNR from 7.5 to 6.0.
- We reprocessed the FAST real dataset of FRB 20190520B using BASSET. The newly detected 79 pulses doubled the number of pulses compared to the previously known 75 pulses, bringing the total to 154. We calibrated the flux densities of the newly detected pulses and updated the energy distribution of FRB 20190520B reported by Niu et al. (2022a) using the new detections.
- BASSET has the potential to expand new parameter space and reveal the intrinsic luminosity function of FRBs.

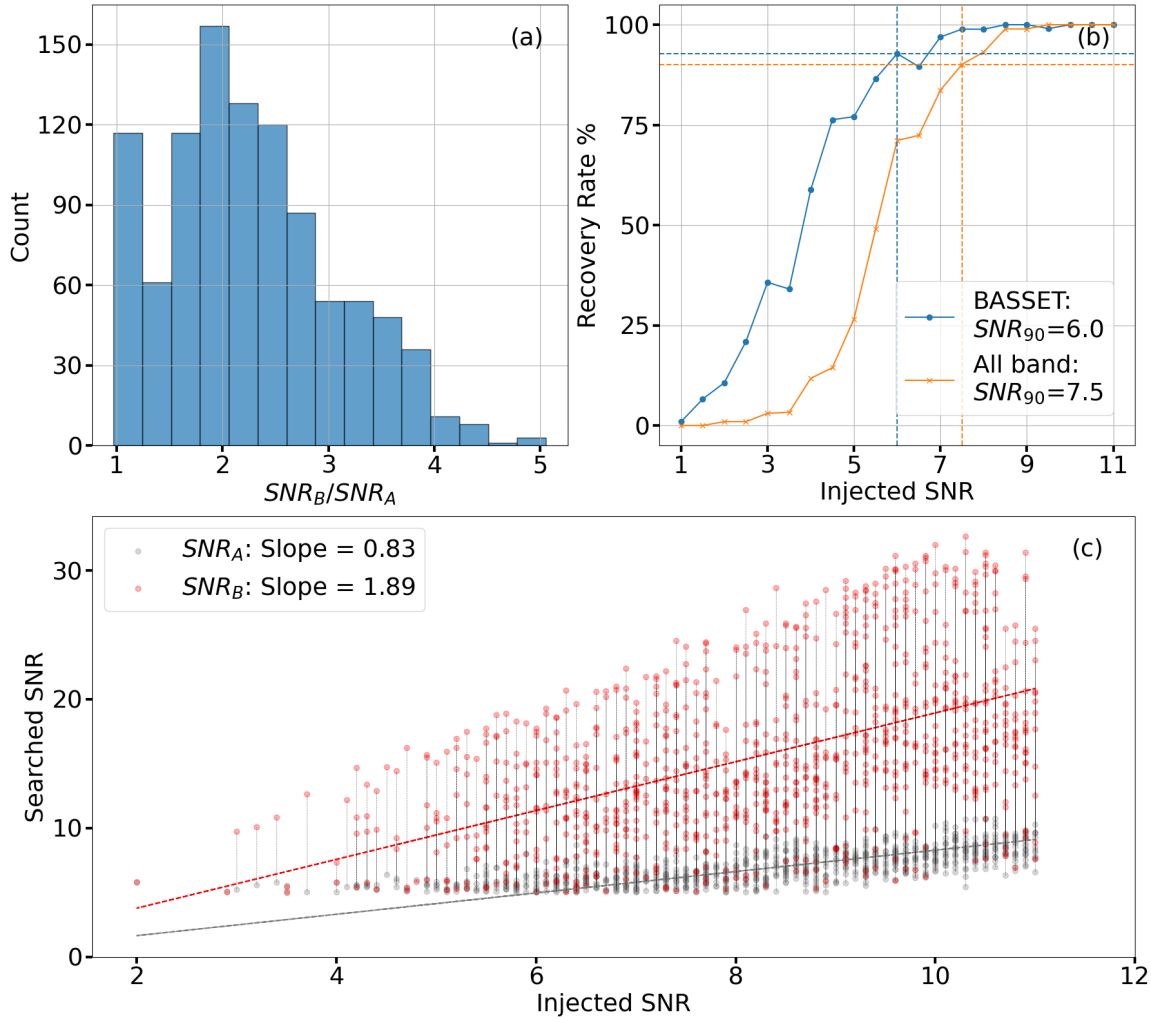


**Figure 10.** Comparison between the BASSET and the standard pipeline. The result is based on 2000 mock pulses. Panel a presents the distribution of the SNR improvement ratio ( $SNR_A/SNR_B$ ). Panel b shows the recovery rate as a function of the injected SNR, where  $SNR_{90}$  represents the 90% completeness threshold. Panel c shows a comparison between  $SNR_A$  and  $SNR_B$ .

1 This work is supported by National Natural Science Foundation of China (NSFC) Programs (Grant No.  
 2 12375236, 12135009, 12203045, 12103013, 12103069, 11988101, 11725313, 11690024, 12041303, 12473047, U1731238,  
 3 12233002, 12041306); by CAS International Partnership Program (No. 114-A11KYSB20160008); by CAS  
 4 Strategic Priority Research Program (No. XDB23000000); by the National Key R&D Program of China  
 5 (No. 2017YFA0402600, 2021YFA0718500); by the National SKA Program of China (No. 2020SKA0120200,  
 6 2022SKA0130100, 2020SKA0120300); by the Leading Innovation and Entrepreneurship Team of Zhejiang Province  
 7 of China (Grant No. 2023R01008); by the Key R&D Program of Zhejiang (Grant No. 2024SSYS0012) and Foundation  
 8 of Guizhou Provincial Education Department (Grants No. KY(2023)059). D.L. is a New Cornerstone investigator.  
 9 P.W. acknowledges support from the CAS Youth Interdisciplinary Team, the Youth Innovation Promotion Association  
 10 CAS (id. 2021055), and the Cultivation Project for FAST Scientific Payoff and Research Achievement of CAMS-CAS.  
 11 E.G. is supported by NSFC programme 11988101 under the foreign talents grant QN2023061004L.

12 This work made use of data from FAST, a Chinese national mega-science facility built and operated by the National  
 13 Astronomical Observatories, Chinese Academy of Sciences.

The data is available at <https://doi.org/10.57760/sciencedb.15289>.

*Facilities:* FAST:500m

*Software:* astropy (Astropy Collaboration et al. 2013, 2018), PRESTO(Ransom 2001), PyAstronomy(Czesla et al. 2019), PyEphem(Rhodes 2011)

## APPENDIX



A. THE NEWLY DETECTED PULSES FROM FRB 20190520B

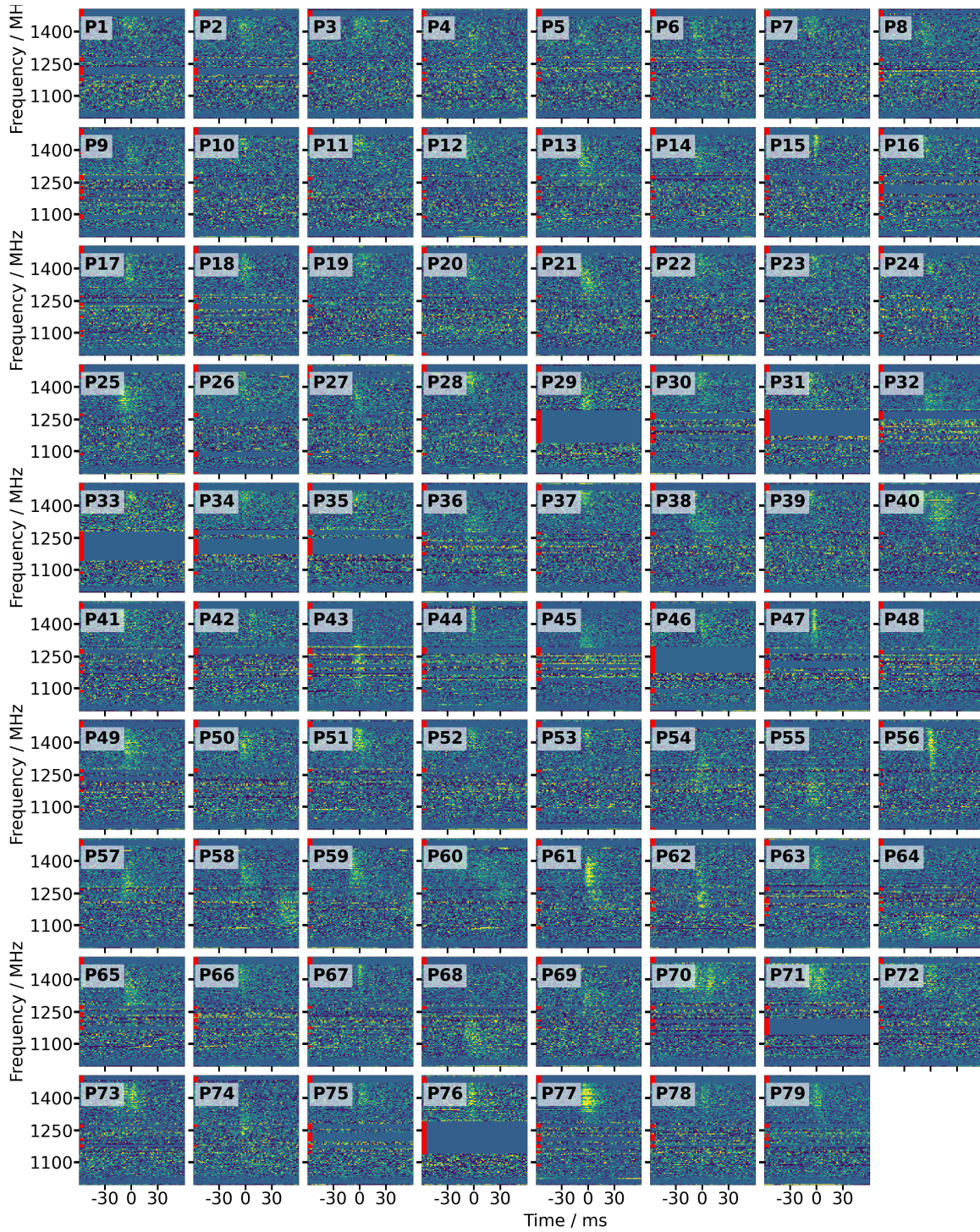


**Figure 11.** The dynamic spectra of the newly detected pulses from FRB 20190520B. The frequency channels affected by RFI are masked and highlighted.

**Table 4.** The properties of the newly detected pulses from FRB 20190520B.

Pulse	MJD <sup>a)</sup>	DM <sup>b)</sup>	W <sub>eq</sub> <sup>c)</sup>	Cntrl freq.	Bandwidth <sup>d)</sup>	Peak flux	Fluence	Energy <sup>e)</sup> <sub>Δν</sub>	SNR <sub>B</sub> <sup>f)</sup>	SNR <sub>A</sub> <sup>f)</sup>
<i>Num</i>	<i>(at infinite freq.)</i>	<i>(pc cm<sup>-3</sup>)</i>	<i>(ms)</i>	<i>(MHz)</i>	<i>(MHz)</i>	<i>(mJy)</i>	<i>(mJy ms)</i>	<i>(×10<sup>37</sup> erg)</i>		
1	58963.77015925	1201.84 <sup>+1.98</sup> <sub>-1.98</sub>	11.9 <sup>+2.8</sup> <sub>-2.8</sub>	1423	148 <sup>+15</sup> <sub>-15</sub> (2)	16.19 <sup>+0.52</sup> <sub>-0.52</sub>	193.14 <sup>+3.94</sup> <sub>-3.94</sub>	4.19 <sup>+2.64</sup> <sub>-2.64</sub>	7.1	4.1
2	58963.77084026	1202.11 <sup>+1.89</sup> <sub>-1.89</sub>	11.0 <sup>+2.3</sup> <sub>-2.3</sub>	1436	160 <sup>+16</sup> <sub>-16</sub> (1)	20.28 <sup>+0.65</sup> <sub>-0.65</sub>	223.52 <sup>+4.58</sup> <sub>-4.58</sub>	5.23 <sup>+0.50</sup> <sub>-0.50</sub>	8.6	5.8
3	58963.80810873	1202.00 <sup>+2.17</sup> <sub>-2.17</sub>	15.6 <sup>+5.6</sup> <sub>-5.6</sub>	1356	134 <sup>+13</sup> <sub>-13</sub> (2)	9.51 <sup>+0.28</sup> <sub>-0.28</sub>	148.41 <sup>+2.80</sup> <sub>-2.80</sub>	2.90 <sup>+2.31</sup> <sub>-2.31</sub>	6.3	3.6
4	58991.67612426	1205.57 <sup>+0.28</sup> <sub>-0.28</sub>	15.8 <sup>+4.8</sup> <sub>-4.8</sub>	1306	118 <sup>+12</sup> <sub>-12</sub> (1)	18.09 <sup>+0.69</sup> <sub>-0.69</sub>	286.26 <sup>+6.92</sup> <sub>-6.92</sub>	4.95 <sup>+0.87</sup> <sub>-0.87</sub>	7.1	5.4
5	58991.67809483	1202.51 <sup>+1.42</sup> <sub>-1.42</sub>	6.9 <sup>+3.0</sup> <sub>-3.0</sub>	1368	111 <sup>+11</sup> <sub>-11</sub> (1)	12.16 <sup>+0.34</sup> <sub>-0.34</sub>	84.37 <sup>+1.51</sup> <sub>-1.51</sub>	1.37 <sup>+0.11</sup> <sub>-0.11</sub>	5.7	4.6
6	58991.68165178	1205.03 <sup>+1.75</sup> <sub>-1.75</sub>	12.6 <sup>+3.0</sup> <sub>-3.0</sub>	1398	220 <sup>+22</sup> <sub>-22</sub> (1)	17.47 <sup>+1.70</sup> <sub>-1.70</sub>	220.24 <sup>+13.62</sup> <sub>-13.62</sub>	7.09 <sup>+0.84</sup> <sub>-0.84</sub>	7.4	5.9
7	58991.68701641	1202.32 <sup>+1.58</sup> <sub>-1.58</sub>	12.1 <sup>+3.2</sup> <sub>-3.2</sub>	1414	134 <sup>+13</sup> <sub>-13</sub> (1)	18.35 <sup>+0.59</sup> <sub>-0.59</sub>	222.87 <sup>+4.54</sup> <sub>-4.54</sub>	4.38 <sup>+0.50</sup> <sub>-0.50</sub>	7.5	5.3
8	58991.68783290	1201.77 <sup>+1.74</sup> <sub>-1.74</sub>	14.5 <sup>+4.0</sup> <sub>-4.0</sub>	1410	162 <sup>+16</sup> <sub>-16</sub> (2)	15.54 <sup>+0.51</sup> <sub>-0.51</sub>	225.10 <sup>+4.68</sup> <sub>-4.68</sub>	5.32 <sup>+0.51</sup> <sub>-0.51</sub>	6.0	4.8
9	58991.70118536	1202.51 <sup>+1.62</sup> <sub>-1.62</sub>	5.4 <sup>+2.7</sup> <sub>-2.7</sub>	1352	66 <sup>+7</sup> <sub>-7</sub> (1)	17.81 <sup>+0.42</sup> <sub>-0.42</sub>	96.59 <sup>+1.44</sup> <sub>-1.44</sub>	0.94 <sup>+0.27</sup> <sub>-0.27</sub>	6.0	4.3
10	58991.73307144	1204.62 <sup>+0.82</sup> <sub>-0.82</sub>	9.6 <sup>+2.5</sup> <sub>-2.5</sub>	1435	130 <sup>+13</sup> <sub>-13</sub> (1)	19.02 <sup>+0.64</sup> <sub>-0.64</sub>	182.74 <sup>+3.90</sup> <sub>-3.90</sub>	3.48 <sup>+0.31</sup> <sub>-0.31</sub>	8.3	3.5
11	58991.73947255	1201.25 <sup>+2.08</sup> <sub>-2.08</sub>	12.3 <sup>+3.0</sup> <sub>-3.0</sub>	1428	104 <sup>+10</sup> <sub>-10</sub> (1)	22.85 <sup>+0.72</sup> <sub>-0.72</sub>	281.46 <sup>+5.63</sup> <sub>-5.63</sub>	4.29 <sup>+0.31</sup> <sub>-0.31</sub>	7.7	4.3
12	59060.47893855	1203.00 <sup>+1.92</sup> <sub>-1.92</sub>	10.9 <sup>+3.8</sup> <sub>-3.8</sub>	1401	169 <sup>+17</sup> <sub>-17</sub> (2)	19.39 <sup>+0.65</sup> <sub>-0.65</sub>	212.25 <sup>+9.04</sup> <sub>-9.04</sub>	5.24 <sup>+0.57</sup> <sub>-0.57</sub>	6.4	3.6
13	59060.48025216	1202.73 <sup>+1.65</sup> <sub>-1.65</sub>	10.6 <sup>+2.2</sup> <sub>-2.2</sub>	1355	102 <sup>+10</sup> <sub>-10</sub> (2)	34.92 <sup>+0.91</sup> <sub>-0.91</sub>	370.64 <sup>+12.24</sup> <sub>-12.24</sub>	5.53 <sup>+1.54</sup> <sub>-1.54</sub>	10.6	7.7
14	59060.48341458	1201.20 <sup>+1.49</sup> <sub>-1.49</sub>	10.7 <sup>+4.1</sup> <sub>-4.1</sub>	1350	170 <sup>+17</sup> <sub>-17</sub> (2)	20.05 <sup>+0.66</sup> <sub>-0.66</sub>	214.20 <sup>+8.98</sup> <sub>-8.98</sub>	5.33 <sup>+2.45</sup> <sub>-2.45</sub>	5.8	4.5
15	59060.48360265	1200.23 <sup>+1.44</sup> <sub>-1.44</sub>	4.8 <sup>+1.5</sup> <sub>-1.5</sub>	1431	131 <sup>+13</sup> <sub>-13</sub> (2)	32.97 <sup>+1.07</sup> <sub>-1.07</sub>	159.19 <sup>+6.55</sup> <sub>-6.55</sub>	3.04 <sup>+0.58</sup> <sub>-0.58</sub>	7.3	6.4
16	59060.50838923	1201.65 <sup>+1.88</sup> <sub>-1.88</sub>	9.9 <sup>+2.8</sup> <sub>-2.8</sub>	1407	161 <sup>+16</sup> <sub>-16</sub> (1)	22.90 <sup>+0.77</sup> <sub>-0.77</sub>	225.65 <sup>+9.69</sup> <sub>-9.69</sub>	5.32 <sup>+0.57</sup> <sub>-0.57</sub>	5.6	5.0
17	59060.52836586	1201.57 <sup>+1.98</sup> <sub>-1.98</sub>	7.7 <sup>+2.0</sup> <sub>-2.0</sub>	1385	243 <sup>+24</sup> <sub>-24</sub> (1)	27.37 <sup>+1.77</sup> <sub>-1.77</sub>	211.50 <sup>+17.36</sup> <sub>-17.36</sub>	7.50 <sup>+0.82</sup> <sub>-0.82</sub>	8.9	7.7
18	59060.52872694	1201.79 <sup>+1.80</sup> <sub>-1.80</sub>	10.8 <sup>+2.8</sup> <sub>-2.8</sub>	1379	285 <sup>+28</sup> <sub>-28</sub> (1)	23.23 <sup>+1.78</sup> <sub>-1.78</sub>	250.38 <sup>+24.43</sup> <sub>-24.43</sub>	10.43 <sup>+1.27</sup> <sub>-1.27</sub>	9.9	7.3
19	59060.52955930	1202.43 <sup>+2.07</sup> <sub>-2.07</sub>	8.1 <sup>+2.8</sup> <sub>-2.8</sub>	1437	210 <sup>+21</sup> <sub>-21</sub> (1)	16.65 <sup>+0.61</sup> <sub>-0.61</sub>	135.26 <sup>+6.29</sup> <sub>-6.29</sub>	4.15 <sup>+0.50</sup> <sub>-0.50</sub>	8.5	4.8
20	59060.53006891	1201.95 <sup>+1.82</sup> <sub>-1.82</sub>	10.1 <sup>+2.8</sup> <sub>-2.8</sub>	1361	146 <sup>+15</sup> <sub>-15</sub> (2)	20.91 <sup>+0.69</sup> <sub>-0.69</sub>	210.56 <sup>+8.81</sup> <sub>-8.81</sub>	4.51 <sup>+1.94</sup> <sub>-1.94</sub>	5.9	4.2
21	59060.53611424	1202.59 <sup>+1.74</sup> <sub>-1.74</sub>	13.4 <sup>+2.9</sup> <sub>-2.9</sub>	1346	313 <sup>+36</sup> <sub>-36</sub> (1)	23.94 <sup>+1.78</sup> <sub>-1.78</sub>	321.33 <sup>+30.27</sup> <sub>-30.27</sub>	14.72 <sup>+1.57</sup> <sub>-1.57</sub>	14.2	10.1
22	59060.53668616	1201.06 <sup>+1.48</sup> <sub>-1.48</sub>	14.0 <sup>+4.4</sup> <sub>-4.4</sub>	1394	136 <sup>+14</sup> <sub>-14</sub> (2)	21.55 <sup>+0.74</sup> <sub>-0.74</sub>	302.59 <sup>+13.24</sup> <sub>-13.24</sub>	6.01 <sup>+1.55</sup> <sub>-1.55</sub>	8.5	4.3
23	59060.54174452	1201.84 <sup>+1.95</sup> <sub>-1.95</sub>	6.9 <sup>+2.8</sup> <sub>-2.8</sub>	1408	188 <sup>+19</sup> <sub>-19</sub> (1)	16.55 <sup>+0.57</sup> <sub>-0.57</sub>	114.33 <sup>+4.98</sup> <sub>-4.98</sub>	3.14 <sup>+0.35</sup> <sub>-0.35</sub>	6.8	3.7
24	59060.54214026	1202.60 <sup>+1.67</sup> <sub>-1.67</sub>	5.5 <sup>+2.0</sup> <sub>-2.0</sub>	1403	102 <sup>+10</sup> <sub>-10</sub> (2)	24.54 <sup>+0.82</sup> <sub>-0.82</sub>	133.87 <sup>+5.65</sup> <sub>-5.65</sub>	2.01 <sup>+0.24</sup> <sub>-0.24</sub>	5.9	3.3
25	59060.54245748	1203.56 <sup>+1.71</sup> <sub>-1.71</sub>	16.1 <sup>+2.6</sup> <sub>-2.6</sub>	1357	243 <sup>+27</sup> <sub>-27</sub> (1)	33.57 <sup>+2.35</sup> <sub>-2.35</sub>	540.72 <sup>+48.14</sup> <sub>-48.14</sub>	19.24 <sup>+1.96</sup> <sub>-1.96</sub>	15.1	10.5
26	59060.54417158	1201.72 <sup>+1.85</sup> <sub>-1.85</sub>	11.6 <sup>+3.9</sup> <sub>-3.9</sub>	1415	156 <sup>+16</sup> <sub>-16</sub> (2)	21.60 <sup>+0.86</sup> <sub>-0.86</sub>	250.75 <sup>+12.64</sup> <sub>-12.64</sub>	5.71 <sup>+0.94</sup> <sub>-0.94</sub>	8.0	4.0
27	59060.54615672	1203.91 <sup>+0.56</sup> <sub>-0.56</sub>	8.6 <sup>+2.7</sup> <sub>-2.7</sub>	1334	213 <sup>+21</sup> <sub>-21</sub> (1)	20.02 <sup>+1.45</sup> <sub>-1.45</sub>	172.19 <sup>+15.81</sup> <sub>-15.81</sub>	5.37 <sup>+0.65</sup> <sub>-0.65</sub>	8.5	5.3
28	59060.54694786	1201.91 <sup>+1.90</sup> <sub>-1.90</sub>	15.1 <sup>+3.0</sup> <sub>-3.0</sub>	1445	187 <sup>+19</sup> <sub>-19</sub> (1)	32.52 <sup>+1.12</sup> <sub>-1.12</sub>	490.07 <sup>+21.50</sup> <sub>-21.50</sub>	13.37 <sup>+1.11</sup> <sub>-1.11</sub>	13.8	7.8
29	59061.49706760	1202.60 <sup>+1.59</sup> <sub>-1.59</sub>	5.5 <sup>+2.6</sup> <sub>-2.6</sub>	1280	218 <sup>+22</sup> <sub>-22</sub> (1)	22.40 <sup>+1.00</sup> <sub>-1.00</sub>	122.37 <sup>+6.95</sup> <sub>-6.95</sub>	3.89 <sup>+0.41</sup> <sub>-0.41</sub>	8.8	5.5

**Table 4.** The properties of the newly detected pulses from FRB 20190520B.

Pulse	MJD <sup>a)</sup>	DM <sup>b)</sup>	W <sub>eq</sub> <sup>c)</sup>	Cntrl freq.	Bandwidth <sup>d)</sup>	Peak flux	Fluence	Energy <sup>e)</sup> <sub>Δν</sub>	SNR <sub>B</sub> <sup>f)</sup>	SNR <sub>A</sub> <sup>f)</sup>
<i>Num</i>	<i>(at infinite freq.)</i>	<i>(pc cm<sup>-3</sup>)</i>	<i>(ms)</i>	<i>(MHz)</i>	<i>(MHz)</i>	<i>(mJy)</i>	<i>(mJy ms)</i>	<i>(×10<sup>37</sup> erg)</i>		
30	59061.50017397	1203.81 <sup>+1.57</sup> <sub>-1.57</sub>	15.9 <sup>+4.1</sup> <sub>-4.1</sub>	1422	57 <sup>+6</sup> <sub>-6</sub> (1)	32.27 <sup>+0.93</sup> <sub>-0.93</sub>	513.57 <sup>+18.87</sup> <sub>-18.87</sub>	4.32 <sup>+1.89</sup> <sub>-1.89</sub>	11.1	8.0
31	59061.50327903	1201.14 <sup>+1.52</sup> <sub>-1.52</sub>	11.4 <sup>+2.6</sup> <sub>-2.6</sub>	1388	139 <sup>+14</sup> <sub>-14</sub> (2)	23.02 <sup>+0.74</sup> <sub>-0.74</sub>	263.16 <sup>+10.76</sup> <sub>-10.76</sub>	5.35 <sup>+0.51</sup> <sub>-0.51</sub>	8.7	5.8
32	59061.50358025	1201.70 <sup>+1.84</sup> <sub>-1.84</sub>	10.4 <sup>+3.7</sup> <sub>-3.7</sub>	1320	271 <sup>+27</sup> <sub>-27</sub> (1)	24.04 <sup>+1.41</sup> <sub>-1.41</sub>	250.91 <sup>+18.73</sup> <sub>-18.73</sub>	9.94 <sup>+1.57</sup> <sub>-1.57</sub>	7.3	5.6
33	59061.50535443	1205.38 <sup>+0.90</sup> <sub>-0.90</sub>	9.4 <sup>+3.0</sup> <sub>-3.0</sub>	1428	113 <sup>+11</sup> <sub>-11</sub> (1)	25.15 <sup>+0.79</sup> <sub>-0.79</sub>	236.21 <sup>+9.38</sup> <sub>-9.38</sub>	3.92 <sup>+0.41</sup> <sub>-0.41</sub>	5.9	3.4
34	59061.50751035	1201.17 <sup>+1.79</sup> <sub>-1.79</sub>	11.4 <sup>+3.8</sup> <sub>-3.8</sub>	1432	86 <sup>+9</sup> <sub>-9</sub> (1)	25.13 <sup>+0.73</sup> <sub>-0.73</sub>	286.56 <sup>+10.62</sup> <sub>-10.62</sub>	3.60 <sup>+0.25</sup> <sub>-0.25</sub>	8.4	6.5
35	59061.51067699	1202.81 <sup>+1.31</sup> <sub>-1.31</sub>	13.3 <sup>+3.7</sup> <sub>-3.7</sub>	1432	116 <sup>+12</sup> <sub>-12</sub> (1)	27.01 <sup>+0.82</sup> <sub>-0.82</sub>	358.05 <sup>+13.74</sup> <sub>-13.74</sub>	6.09 <sup>+1.45</sup> <sub>-1.45</sub>	6.1	4.2
36	59061.51889186	1202.36 <sup>+1.85</sup> <sub>-1.85</sub>	13.0 <sup>+5.3</sup> <sub>-5.3</sub>	1319	130 <sup>+13</sup> <sub>-13</sub> (2)	22.81 <sup>+1.11</sup> <sub>-1.11</sub>	297.36 <sup>+18.39</sup> <sub>-18.39</sub>	5.64 <sup>+0.57</sup> <sub>-0.57</sub>	6.2	4.1
37	59061.52526941	1200.56 <sup>+1.48</sup> <sub>-1.48</sub>	9.6 <sup>+2.3</sup> <sub>-2.3</sub>	1470	193 <sup>+19</sup> <sub>-19</sub> (1)	23.75 <sup>+0.77</sup> <sub>-0.77</sub>	228.95 <sup>+9.43</sup> <sub>-9.43</sub>	6.47 <sup>+0.97</sup> <sub>-0.97</sub>	11.2	7.8
38	59061.53097863	1201.52 <sup>+1.56</sup> <sub>-1.56</sub>	12.8 <sup>+3.8</sup> <sub>-3.8</sub>	1323	147 <sup>+15</sup> <sub>-15</sub> (2)	22.38 <sup>+1.12</sup> <sub>-1.12</sub>	285.42 <sup>+18.11</sup> <sub>-18.11</sub>	6.13 <sup>+0.67</sup> <sub>-0.67</sub>	10.3	3.6
39	59061.53278232	1203.60 <sup>+1.24</sup> <sub>-1.24</sub>	7.1 <sup>+3.1</sup> <sub>-3.1</sub>	1426	140 <sup>+14</sup> <sub>-14</sub> (1)	19.47 <sup>+0.63</sup> <sub>-0.63</sub>	138.66 <sup>+5.70</sup> <sub>-5.70</sub>	2.83 <sup>+0.32</sup> <sub>-0.32</sub>	6.4	4.5
40	59061.54840199	1203.37 <sup>+4.02</sup> <sub>-4.02</sub>	28.8 <sup>+6.3</sup> <sub>-6.3</sub>	1345	305 <sup>+30</sup> <sub>-30</sub> (2)	24.29 <sup>+1.72</sup> <sub>-1.72</sub>	700.01 <sup>+62.87</sup> <sub>-62.87</sub>	31.17 <sup>+3.46</sup> <sub>-3.46</sub>	8.1	6.5
41	59067.46362248	1202.50 <sup>+1.98</sup> <sub>-1.98</sub>	12.2 <sup>+4.2</sup> <sub>-4.2</sub>	1442	92 <sup>+9</sup> <sub>-9</sub> (2)	25.70 <sup>+0.77</sup> <sub>-0.77</sub>	313.39 <sup>+11.97</sup> <sub>-11.97</sub>	4.20 <sup>+0.69</sup> <sub>-0.69</sub>	7.2	5.7
42	59067.47196287	1201.75 <sup>+1.87</sup> <sub>-1.87</sub>	8.6 <sup>+3.2</sup> <sub>-3.2</sub>	1436	47 <sup>+5</sup> <sub>-5</sub> (1)	32.37 <sup>+0.81</sup> <sub>-0.81</sub>	277.86 <sup>+8.88</sup> <sub>-8.88</sub>	1.90 <sup>+0.21</sup> <sub>-0.21</sub>	6.4	4.2
43	59067.48018037	1203.08 <sup>+1.81</sup> <sub>-1.81</sub>	3.5 <sup>+2.5</sup> <sub>-2.5</sub>	1255	150 <sup>+15</sup> <sub>-15</sub> (1)	29.22 <sup>+1.62</sup> <sub>-1.62</sub>	101.83 <sup>+7.17</sup> <sub>-7.17</sub>	2.24 <sup>+0.31</sup> <sub>-0.31</sub>	10.5	8.1
44	59067.48114672	1203.99 <sup>+0.69</sup> <sub>-0.69</sub>	5.7 <sup>+1.3</sup> <sub>-1.3</sub>	1427	209 <sup>+53</sup> <sub>-53</sub> (1)	30.03 <sup>+1.05</sup> <sub>-1.05</sub>	170.94 <sup>+7.56</sup> <sub>-7.56</sub>	5.21 <sup>+0.63</sup> <sub>-0.63</sub>	16.0	10.8
45	59067.48472680	1201.74 <sup>+1.98</sup> <sub>-1.98</sub>	7.3 <sup>+2.8</sup> <sub>-2.8</sub>	1284	125 <sup>+13</sup> <sub>-13</sub> (1)	43.75 <sup>+2.23</sup> <sub>-2.23</sub>	318.49 <sup>+20.58</sup> <sub>-20.58</sub>	5.84 <sup>+0.76</sup> <sub>-0.76</sub>	7.5	6.3
46	59067.48919208	1199.76 <sup>+1.58</sup> <sub>-1.58</sub>	8.5 <sup>+4.1</sup> <sub>-4.1</sub>	1378	233 <sup>+23</sup> <sub>-23</sub> (1)	23.11 <sup>+1.71</sup> <sub>-1.71</sub>	195.47 <sup>+18.32</sup> <sub>-18.32</sub>	6.66 <sup>+0.93</sup> <sub>-0.93</sub>	6.8	4.7
47	59067.48943302	1201.86 <sup>+1.99</sup> <sub>-1.99</sub>	5.6 <sup>+0.8</sup> <sub>-0.8</sub>	1391	158 <sup>+7</sup> <sub>-7</sub> (2)	49.60 <sup>+1.64</sup> <sub>-1.64</sub>	277.68 <sup>+11.69</sup> <sub>-11.69</sub>	6.43 <sup>+0.39</sup> <sub>-0.39</sub>	17.2	11.9
48	59067.49143691	1202.80 <sup>+1.89</sup> <sub>-1.89</sub>	11.9 <sup>+3.4</sup> <sub>-3.4</sub>	1390	181 <sup>+18</sup> <sub>-18</sub> (2)	18.55 <sup>+0.59</sup> <sub>-0.59</sub>	221.24 <sup>+8.98</sup> <sub>-8.98</sub>	5.84 <sup>+1.07</sup> <sub>-1.07</sub>	8.1	5.9
49	59067.50320604	1201.08 <sup>+1.46</sup> <sub>-1.46</sub>	17.9 <sup>+2.6</sup> <sub>-2.6</sub>	1382	146 <sup>+15</sup> <sub>-15</sub> (2)	35.60 <sup>+1.14</sup> <sub>-1.14</sub>	637.65 <sup>+25.94</sup> <sub>-25.94</sub>	13.65 <sup>+0.68</sup> <sub>-0.68</sub>	11.9	8.6
50	59067.50475553	1202.20 <sup>+1.89</sup> <sub>-1.89</sub>	9.4 <sup>+2.4</sup> <sub>-2.4</sub>	1395	243 <sup>+24</sup> <sub>-24</sub> (1)	28.44 <sup>+1.62</sup> <sub>-1.62</sub>	268.47 <sup>+19.43</sup> <sub>-19.43</sub>	9.54 <sup>+1.23</sup> <sub>-1.23</sub>	11.5	7.0
51	59067.50694658	1204.42 <sup>+1.32</sup> <sub>-1.32</sub>	13.2 <sup>+1.9</sup> <sub>-1.9</sub>	1400	129 <sup>+13</sup> <sub>-13</sub> (2)	40.97 <sup>+1.44</sup> <sub>-1.44</sub>	538.88 <sup>+24.06</sup> <sub>-24.06</sub>	10.19 <sup>+1.69</sup> <sub>-1.69</sub>	13.6	9.0
52	59067.51160959	1201.35 <sup>+1.71</sup> <sub>-1.71</sub>	8.6 <sup>+2.7</sup> <sub>-2.7</sub>	1404	161 <sup>+16</sup> <sub>-16</sub> (2)	21.48 <sup>+0.74</sup> <sub>-0.74</sub>	184.78 <sup>+8.04</sup> <sub>-8.04</sub>	4.35 <sup>+0.68</sup> <sub>-0.68</sub>	7.8	4.0
53	59067.51809977	1201.94 <sup>+1.90</sup> <sub>-1.90</sub>	5.9 <sup>+1.8</sup> <sub>-1.8</sub>	1424	97 <sup>+10</sup> <sub>-10</sub> (1)	29.65 <sup>+0.92</sup> <sub>-0.92</sub>	175.87 <sup>+6.91</sup> <sub>-6.91</sub>	2.49 <sup>+0.40</sup> <sub>-0.40</sub>	7.9	5.6
54	59067.51855025	1201.72 <sup>+1.91</sup> <sub>-1.91</sub>	14.1 <sup>+3.9</sup> <sub>-3.9</sub>	1270	123 <sup>+12</sup> <sub>-12</sub> (1)	28.56 <sup>+1.53</sup> <sub>-1.53</sub>	402.14 <sup>+27.39</sup> <sub>-27.39</sub>	7.24 <sup>+0.62</sup> <sub>-0.62</sub>	6.1	4.2
55	59067.51888109	1201.47 <sup>+1.10</sup> <sub>-1.10</sub>	9.2 <sup>+2.3</sup> <sub>-2.3</sub>	1193	353 <sup>+35</sup> <sub>-35</sub> (1)	19.43 <sup>+0.88</sup> <sub>-0.88</sub>	178.33 <sup>+10.28</sup> <sub>-10.28</sub>	9.22 <sup>+0.71</sup> <sub>-0.71</sub>	8.1	6.9
56	59067.52572300	1204.86 <sup>+0.97</sup> <sub>-0.97</sub>	6.6 <sup>+1.3</sup> <sub>-1.3</sub>	1390	365 <sup>+67</sup> <sub>-67</sub> (1)	30.08 <sup>+2.02</sup> <sub>-2.02</sub>	197.50 <sup>+16.87</sup> <sub>-16.87</sub>	10.53 <sup>+1.22</sup> <sub>-1.22</sub>	17.0	12.1
57	59067.52790177	1198.76 <sup>+0.75</sup> <sub>-0.75</sub>	15.6 <sup>+4.5</sup> <sub>-4.5</sub>	1287	232 <sup>+23</sup> <sub>-23</sub> (1)	23.17 <sup>+1.36</sup> <sub>-1.36</sub>	361.10 <sup>+26.82</sup> <sub>-26.82</sub>	12.25 <sup>+1.07</sup> <sub>-1.07</sub>	8.4	5.9
58	59067.52795093	1203.76 <sup>+4.44</sup> <sub>-4.44</sub>	22.0 <sup>+4.4</sup> <sub>-4.4</sub>	1199	394 <sup>+39</sup> <sub>-39</sub> (1)	22.88 <sup>+1.17</sup> <sub>-1.17</sub>	503.46 <sup>+32.72</sup> <sub>-32.72</sub>	28.98 <sup>+2.80</sup> <sub>-2.80</sub>	11.4	9.1

**Table 4.** The properties of the newly detected pulses from FRB 20190520B.

Pulse	MJD <sup>a)</sup>	DM <sup>b)</sup>	W <sub>eq</sub> <sup>c)</sup>	Cntrl freq.	Bandwidth <sup>d)</sup>	Peak flux	Fluence	Energy <sup>e)</sup> <sub>Δν</sub>	SNR <sub>B</sub> <sup>f)</sup>	SNR <sub>A</sub> <sup>f)</sup>
<i>Num</i>	<i>(at infinite freq.)</i>	<i>(pc cm<sup>-3</sup>)</i>	<i>(ms)</i>	<i>(MHz)</i>	<i>(MHz)</i>	<i>(mJy)</i>	<i>(mJy ms)</i>	<i>(×10<sup>37</sup> erg)</i>		
59	59067.52812338	1201.84 <sup>+2.07</sup> <sub>-2.07</sub>	9.2 <sup>+2.3</sup> <sub>-2.3</sub>	1327	352 <sup>+35</sup> <sub>-35</sub> (1)	21.40 <sup>+1.44</sup> <sub>-1.44</sub>	196.93 <sup>+16.85</sup> <sub>-16.85</sub>	10.12 <sup>+1.02</sup> <sub>-1.02</sub>	11.9	8.9
60	59067.52833961	1201.59 <sup>+4.76</sup> <sub>-4.76</sub>	28.6 <sup>+7.5</sup> <sub>-7.5</sub>	1376	127 <sup>+13</sup> <sub>-13</sub> (2)	24.16 <sup>+0.83</sup> <sub>-0.83</sub>	689.75 <sup>+30.19</sup> <sub>-30.19</sub>	12.83 <sup>+1.62</sup> <sub>-1.62</sub>	5.1	4.5
61	59067.53192495	1202.55 <sup>+1.92</sup> <sub>-1.92</sub>	10.8 <sup>+1.6</sup> <sub>-1.6</sub>	1338	392 <sup>+38</sup> <sub>-38</sub> (1)	33.11 <sup>+2.18</sup> <sub>-2.18</sub>	358.15 <sup>+30.01</sup> <sub>-30.01</sub>	20.52 <sup>+1.91</sup> <sub>-1.91</sub>	16.6	12.6
62	59077.43170549	1200.04 <sup>+1.14</sup> <sub>-1.14</sub>	8.9 <sup>+2.9</sup> <sub>-2.9</sub>	1249	135 <sup>+14</sup> <sub>-14</sub> (2)	26.92 <sup>+1.06</sup> <sub>-1.06</sub>	240.59 <sup>+11.98</sup> <sub>-11.98</sub>	4.75 <sup>+1.47</sup> <sub>-1.47</sub>	9.4	8.9
63	59077.46064368	1201.53 <sup>+1.91</sup> <sub>-1.91</sub>	6.9 <sup>+3.5</sup> <sub>-3.5</sub>	1396	257 <sup>+26</sup> <sub>-26</sub> (1)	26.12 <sup>+1.39</sup> <sub>-1.39</sub>	179.23 <sup>+12.10</sup> <sub>-12.10</sub>	6.74 <sup>+0.67</sup> <sub>-0.67</sub>	9.2	7.0
64	59077.46596665	1200.95 <sup>+1.63</sup> <sub>-1.63</sub>	11.6 <sup>+4.4</sup> <sub>-4.4</sub>	1075	230 <sup>+23</sup> <sub>-23</sub> (1)	22.50 <sup>+0.65</sup> <sub>-0.65</sub>	261.37 <sup>+9.66</sup> <sub>-9.66</sub>	8.77 <sup>+0.72</sup> <sub>-0.72</sub>	7.2	4.8
65	59077.46688247	1203.02 <sup>+1.60</sup> <sub>-1.60</sub>	8.2 <sup>+3.0</sup> <sub>-3.0</sub>	1320	380 <sup>+38</sup> <sub>-38</sub> (1)	15.28 <sup>+0.79</sup> <sub>-0.79</sub>	125.19 <sup>+8.20</sup> <sub>-8.20</sub>	6.96 <sup>+0.55</sup> <sub>-0.55</sub>	10.7	7.1
66	59077.47341161	1202.81 <sup>+1.80</sup> <sub>-1.80</sub>	10.2 <sup>+2.4</sup> <sub>-2.4</sub>	1414	170 <sup>+17</sup> <sub>-17</sub> (2)	24.10 <sup>+0.80</sup> <sub>-0.80</sub>	246.49 <sup>+10.40</sup> <sub>-10.40</sub>	6.13 <sup>+0.36</sup> <sub>-0.36</sub>	9.0	4.4
67	59077.47762721	1199.90 <sup>+1.39</sup> <sub>-1.39</sub>	6.2 <sup>+1.8</sup> <sub>-1.8</sub>	1428	137 <sup>+14</sup> <sub>-14</sub> (2)	30.67 <sup>+1.01</sup> <sub>-1.01</sub>	188.83 <sup>+7.90</sup> <sub>-7.90</sub>	3.77 <sup>+0.52</sup> <sub>-0.52</sub>	10.6	7.4
68	59077.48005306	1200.99 <sup>+2.25</sup> <sub>-2.25</sub>	13.6 <sup>+3.3</sup> <sub>-3.3</sub>	1138	194 <sup>+19</sup> <sub>-19</sub> (2)	27.20 <sup>+0.72</sup> <sub>-0.72</sub>	371.14 <sup>+12.56</sup> <sub>-12.56</sub>	10.55 <sup>+0.95</sup> <sub>-0.95</sub>	6.7	5.6
69	59077.48829166	1202.37 <sup>+1.90</sup> <sub>-1.90</sub>	9.7 <sup>+2.9</sup> <sub>-2.9</sub>	1290	196 <sup>+20</sup> <sub>-20</sub> (2)	22.00 <sup>+1.02</sup> <sub>-1.02</sub>	213.82 <sup>+12.62</sup> <sub>-12.62</sub>	6.12 <sup>+0.44</sup> <sub>-0.44</sub>	6.6	4.5
70	59089.42255268	1202.71 <sup>+4.08</sup> <sub>-4.08</sub>	31.3 <sup>+2.6</sup> <sub>-2.6</sub>	1402	121 <sup>+12</sup> <sub>-12</sub> (2)	37.39 <sup>+1.44</sup> <sub>-1.44</sub>	1170.41 <sup>+14.29</sup> <sub>-14.29</sub>	20.64 <sup>+1.99</sup> <sub>-1.99</sub>	18.4	11.7
71	59089.42638332	1202.47 <sup>+3.64</sup> <sub>-3.64</sub>	24.6 <sup>+2.3</sup> <sub>-2.3</sub>	1396	214 <sup>+21</sup> <sub>-21</sub> (1)	25.25 <sup>+0.98</sup> <sub>-0.98</sub>	620.72 <sup>+7.69</sup> <sub>-7.69</sub>	19.44 <sup>+2.30</sup> <sub>-2.30</sub>	19.0	8.1
72	59089.44362517	1202.58 <sup>+4.56</sup> <sub>-4.56</sub>	17.5 <sup>+3.8</sup> <sub>-3.8</sub>	1399	106 <sup>+11</sup> <sub>-11</sub> (2)	18.50 <sup>+0.61</sup> <sub>-0.61</sub>	324.46 <sup>+3.38</sup> <sub>-3.38</sub>	5.04 <sup>+1.33</sup> <sub>-1.33</sub>	11.3	8.3
73	59089.44381959	1202.25 <sup>+4.69</sup> <sub>-4.69</sub>	19.5 <sup>+2.1</sup> <sub>-2.1</sub>	1388	154 <sup>+6</sup> <sub>-6</sub> (2)	31.72 <sup>+1.04</sup> <sub>-1.04</sub>	617.81 <sup>+6.43</sup> <sub>-6.43</sub>	13.91 <sup>+0.52</sup> <sub>-0.52</sub>	16.8	11.8
74	59089.45120231	1205.94 <sup>+2.67</sup> <sub>-2.67</sub>	10.3 <sup>+4.1</sup> <sub>-4.1</sub>	1269	341 <sup>+34</sup> <sub>-34</sub> (1)	10.25 <sup>+0.65</sup> <sub>-0.65</sub>	105.19 <sup>+2.11</sup> <sub>-2.11</sub>	5.25 <sup>+0.41</sup> <sub>-0.41</sub>	11.1	9.3
75	59111.36402893	1202.22 <sup>+4.42</sup> <sub>-4.42</sub>	11.9 <sup>+3.7</sup> <sub>-3.7</sub>	1389	221 <sup>+22</sup> <sub>-22</sub> (2)	12.76 <sup>+0.54</sup> <sub>-0.54</sub>	151.20 <sup>+4.10</sup> <sub>-4.10</sub>	4.88 <sup>+4.32</sup> <sub>-4.32</sub>	8.3	5.2
76	59111.36526831	1201.45 <sup>+1.72</sup> <sub>-1.72</sub>	17.3 <sup>+3.6</sup> <sub>-3.6</sub>	1398	151 <sup>+15</sup> <sub>-15</sub> (1)	16.49 <sup>+0.52</sup> <sub>-0.52</sub>	284.48 <sup>+5.74</sup> <sub>-5.74</sub>	6.29 <sup>+3.40</sup> <sub>-3.40</sub>	9.8	7.6
77	59111.36856187	1203.11 <sup>+1.63</sup> <sub>-1.63</sub>	14.7 <sup>+1.0</sup> <sub>-1.0</sub>	1393	220 <sup>+19</sup> <sub>-19</sub> (1)	55.27 <sup>+2.29</sup> <sub>-2.29</sub>	811.03 <sup>+21.41</sup> <sub>-21.41</sub>	26.03 <sup>+1.22</sup> <sub>-1.22</sub>	29.1	19.5
78	59111.37352919	1202.87 <sup>+1.71</sup> <sub>-1.71</sub>	9.4 <sup>+2.2</sup> <sub>-2.2</sub>	1403	216 <sup>+22</sup> <sub>-22</sub> (1)	18.43 <sup>+0.76</sup> <sub>-0.76</sub>	173.94 <sup>+4.55</sup> <sub>-4.55</sub>	5.50 <sup>+0.57</sup> <sub>-0.57</sub>	7.7	6.0
79	59111.37932233	1200.55 <sup>+1.64</sup> <sub>-1.64</sub>	11.2 <sup>+1.7</sup> <sub>-1.7</sub>	1375	187 <sup>+19</sup> <sub>-19</sub> (2)	23.60 <sup>+0.99</sup> <sub>-0.99</sub>	264.41 <sup>+7.08</sup> <sub>-7.08</sub>	7.23 <sup>+0.66</sup> <sub>-0.66</sub>	12.5	8.8

a) The time of arrival of the pulses, corrected to an infinite frequency.

b) The structure-optimized DM measured by using the DM-Power algorithm (Lin et al. 2022) (available at <https://github.com/hsiuhsil/DM-power>).

c) The equivalent width, W<sub>eq</sub>, is defined as the width of a rectangular pulse that has an area equal to the integral of the observed pulse and a height matching the peak flux density.

d) Two methods are employed to measure the bandwidth: #1) Fitting a Gaussian function to the pulse's bandpass to determine the bandwidth, with the 1σ measurement uncertainty. #2) Calculating the cumulative distribution function (CDF) of the bandpass and determining the bandwidth based on the derivative of the CDF with respect to

the frequency, with the  $1\sigma$  measurement uncertainty obtained through bootstrapping. For pulses with  $SNR_A \leq 10$ , a conservative estimate of uncertainty of 20% is assumed.

e) The equivalent isotropic energies of the pulses are calculated as described in equation (9) of Zhang (2018) (see Eq. (15)).

f) The  $SNR_A$  and  $SNR_B$  are obtained using `single_pulse_search.py` from PRESTO, which searches the two time series created separately by the BASSET and the standard pipeline.

## REFERENCES

- Aggarwal, K., Agarwal, D., Lewis, E. F., et al. 2021, *The Astrophysical Journal*, 922, 115
- Amiri, M., Bandura, K., Berger, P., et al. 2018, *The Astrophysical Journal*, 863, 48
- Anna-Thomas, R., Connor, L., Dai, S., et al. 2023, *Science*, 380, 599
- Astropy Collaboration, Robitaille, T. P., Tollerud, E. J., et al. 2013, *A&A*, 558, A33, doi: [10.1051/0004-6361/201322068](https://doi.org/10.1051/0004-6361/201322068)
- Astropy Collaboration, Price-Whelan, A. M., Sipőcz, B. M., et al. 2018, *AJ*, 156, 123, doi: [10.3847/1538-3881/aabc4f](https://doi.org/10.3847/1538-3881/aabc4f)
- Bannister, K. W., Shannon, R., Macquart, J.-P., et al. 2017, *The Astrophysical Journal Letters*, 841, L12
- Caleb, M., Flynn, C., Bailes, M., et al. 2017, *Monthly Notices of the Royal Astronomical Society*, 468, 3746
- Champion, D., Petroff, E., Kramer, M., et al. 2016, *Monthly Notices of the Royal Astronomical Society: Letters*, 460, L30
- Cordes, J. M., & Chatterjee, S. 2019, *Annual Review of Astronomy and Astrophysics*, 57, 417
- Czesla, S., Schröter, S., Schneider, C. P., et al. 2019, *PyA: Python astronomy-related packages*. <http://ascl.net/1906.010>
- Gourdji, K., Michilli, D., Spitler, L., et al. 2019, *The Astrophysical Journal Letters*, 877, L19
- Jiang, J.-C., Wang, W.-Y., Xu, H., et al. 2022, *Research in Astronomy and Astrophysics*, 22, 124003
- Kumar, P., Zackay, B., & Law, C. J. 2024, *The Astrophysical Journal*, 960, 128
- Li, D., Wang, P., Qian, L., et al. 2018, *IEEE Microwave Magazine*, 19, 112
- Li, D., Wang, P., Zhu, W., et al. 2021, *Nature*, 598, 267
- Lin, H.-H., Main, R., Pen, U.-L., et al. 2022, arXiv preprint arXiv:2208.13677
- Macquart, J.-P., Prochaska, J., McQuinn, M., et al. 2020, *Nature*, 581, 391
- Marthi, V., Bethapudi, S., Main, R., et al. 2022, *Monthly Notices of the Royal Astronomical Society*, 509, 2209
- Mckinven, R., Gaensler, B., Michilli, D., et al. 2023, *The Astrophysical Journal*, 950, 12
- Men, Y., & Barr, E. 2024, arXiv preprint arXiv:2401.13834
- Michilli, D., Seymour, A., Hessels, J., et al. 2018, *Nature*, 553, 182
- Nan, R., Li, D., Jin, C., et al. 2011, *International Journal of Modern Physics D*, 20, 989
- Niu, C.-H., Aggarwal, K., Li, D., et al. 2022a, *Nature*, 606, 873
- Niu, J.-R., Zhu, W.-W., Zhang, B., et al. 2022b, *Research in Astronomy and Astrophysics*, 22, 124004
- O’Neil, K. 2002, arXiv preprint astro-ph/0203001
- Petroff, E., Hessels, J., & Lorimer, D. 2019, *The Astronomy and Astrophysics Review*, 27, 4
- Pleunis, Z., Good, D. C., Kaspi, V. M., et al. 2021, *The Astrophysical Journal*, 923, 1
- Ransom, S. M. 2001, *New search techniques for binary pulsars* (Harvard University)
- Rhodes, B. C. 2011, *Astrophysics Source Code Library*, ascl
- Spitler, L., Cordes, J., Chatterjee, S., & Stone, J. 2012, *The Astrophysical Journal*, 748, 73
- Spitler, L., Cordes, J. M., Hessels, J., et al. 2014, *The Astrophysical Journal*, 790, 101
- Spitler, L., Scholz, P., Hessels, J., et al. 2016, *Nature*, 531, 202
- Thornton, D. e., Stappers, B., Bailes, M., et al. 2013, *Science*, 341, 53
- Xiao, D., Wang, F., & Dai, Z. 2021, *Science China Physics, Mechanics & Astronomy*, 64, 249501
- Xu, H., Niu, J., Chen, P., et al. 2022, *Nature*, 609, 685
- Xu, J., Feng, Y., Li, D., et al. 2023, *Universe*, 9, 330
- Zackay, B., & Ofek, E. O. 2017, *The Astrophysical Journal*, 835, 11
- Zhang, B. 2018, *The Astrophysical Journal Letters*, 867, L21
- . 2020, *Nature*, 587, 45
- . 2023, *Reviews of Modern Physics*, 95, 035005

Zhang, Y.-K., Wang, P., Feng, Y., et al. 2022, Research in  
Astronomy and Astrophysics, 22, 124002

Zhang, Y.-K., Li, D., Zhang, B., et al. 2023, The  
Astrophysical Journal, 955, 142

Zhou, D., Han, J., Zhang, B., et al. 2022, Research in  
Astronomy and Astrophysics, 22, 124001